The Astrophysical Journal Letters, 989:L22 (26pp), 2025 August 20 https://doi.org/10.3847/2041-8213/adf53f

Worlds Next Door: A Candidate Giant Planet Imaged in the Habitable Zone of α Centauri A. I. Observations, Orbital and Physical Properties, and Exozodi Upper Limits

Charles Beichman[1,2,21], Aniket Sanghi[3,4,21], Dimitri Mawet[2,3], Pierre Kervella[5,6], Kevin Wagner[7], Billy Quarles[8], Jack J. Lissauer[9], Max Sommer[10], Mark Wyatt[10], Nicolas Godoy[11], William O. Balmer[12,13], Laurent Pueyo[13], Jorge Llop-Sayson[2], Jonathan Aguilar[13], Rachel Akeson[1], Ruslan Belikov[9], Anthony Boccaletti[5], Elodie Choquet[11], Edward Fomalont[14,15], Thomas Henning[16], Dean Hines[13], Renyu Hu[2], Pierre-Olivier Lagage[17], Jarron Leisenring[18], James Mang[4,19], Michael Ressler[2], Eugene Serabyn[2], Pascal Tremblin[20], Marie Ygouf[2], and Mantas Zilinskas[2]

[1] NASA Exoplanet Science Institute, Infrared Processing and Analysis Center, California Institute of Technology, Pasadena, CA 91125, USA; chas@ipac.caltech.edu
[2] Jet Propulsion Laboratory, California Institute of Technology, Pasadena, CA 91109, USA
[3] Cahill Center for Astronomy and Astrophysics, California Institute of Technology, 1200 East California Boulevard, MC 249-17, Pasadena, CA 91125, USA; asanghi@caltech.edu
[4] NSF Graduate Research Fellow
[5] LIRA, Observatoire de Paris, Université PSL, Sorbonne Université, Université Paris Cité, CY Cergy Paris Université, CNRS, 5 place Jules Janssen, 92195 Meudon, France
[6] French-Chilean Laboratory for Astronomy, IRL 3386, CNRS, Universidad de Chile, Casilla 36-D, Santiago, Chile
[7] Department of Astronomy and Steward Observatory, University of Arizona, USA
[8] Department of Physics and Astronomy, East Texas A&M University Commerce, TX 75428, USA
[9] Space Science & Astrobiology Division, Building 245, NASA Ames Research Center, Moffett Field, CA 94035, USA
[10] Institute of Astronomy, University of Cambridge, Madingley Road, Cambridge CB3 0HA, UK
[11] Aix Marseille Université, CNRS, CNES, LAM, Marseille, France
[12] Department of Physics & Astronomy, Johns Hopkins University, 3400 North Charles Street, Baltimore, MD 21218, USA
[13] Space Telescope Science Institute, 3700 San Martin Drive, Baltimore, MD 21218, USA
[14] National Radio Astronomy Observatory, 520 Edgemont Road, Charlottesville, VA 22903, USA
[15] ALMA, Vitacura, Santiago, Chile
[16] Max-Planck-Institut für Astronomie (MPIA), Königstuhl 17, 69117 Heidelberg, Germany
[17] Université Paris-Saclay, Université Paris Cité, CEA, CNRS, AIM, 91191 Gif-sur-Yvette, France
[18] Steward Observatory, University of Arizona, Tucson, AZ 85721, USA
[19] Department of Astronomy, University of Texas at Austin, Austin, TX 78712, USA
[20] Université Paris-Saclay, UVSQ, CNRS, CEA, Maison de la Simulation, 91191 Gif-sur-Yvette, France
Received 2025 June 28; revised 2025 July 23; accepted 2025 July 24; published 2025 August 11

Abstract

We report on coronagraphic observations of the nearest solar-type star, α Centauri A (α Cen A), using the MIRI instrument on the James Webb Space Telescope. The proximity of α Cen (1.33 pc) means that the star's habitable zone is spatially resolved at mid-infrared wavelengths, so sufficiently large planets or quantities of exozodiacal dust would be detectable via direct imaging. With three epochs of observation (2024 August, 2025 February, and 2025 April), we achieve a sensitivity sufficient to detect $T_{\rm eff} \approx$ 225–250 K (1–1.2 $R_{\rm Jup}$) planets between $1''$–$2''$ and exozodiacal dust emission at the level of >5–8× the brightness of our own zodiacal cloud. The lack of exozodiacal dust emission sets an unprecedented limit of a few times the brightness of our own zodiacal cloud—a factor of $\gtrsim$10 more sensitive than measured toward any other stellar system to date. In 2024 August, we detected an $F_\nu(15.5\ \mu\text{m}) = 3.5$ mJy point source, called $S1$, at a separation of $1\overset{''}{.}5$ from α Cen A at a contrast level of 5.5×10^{-5}. Because the 2024 August epoch had only one successful observation at a single roll angle, it is not possible to unambiguously confirm $S1$ as a bona fide planet. Our analysis confirms that $S1$ is neither a background nor a foreground object. $S1$ is not recovered in the 2025 February and April epochs. However, if $S1$ is the counterpart of the object $C1$, seen by the Very Large Telescope/New Earths in Alpha Centauri Region program in 2019, we find that there is a 52% chance that the $S1 + C1$ candidate was missed in both follow-up JWST/MIRI observations due to orbital motion. Incorporating constraints from the nondetections, we obtain families of dynamically stable orbits for $S1 + C1$ with periods between 2 and 3 yr. These suggest that the planet candidate is on an eccentric ($e \approx 0.4$) orbit significantly inclined with respect to the α Cen AB orbital plane ($i_{\rm mutual} \approx 50^\circ$, prograde, or $\approx 130^\circ$, retrograde). Based on the photometry and inferred orbital properties, the planet candidate could have a temperature of 225 K, a radius of $\approx$1–1.1 $R_{\rm Jup}$, and a mass between 90 and 150 $M_\oplus$, consistent with radial velocity limits. This Letter is first in a series of two

[21] Shared first authorship.

papers: Paper II discusses the data reduction strategy and finds that $S1$ is robust as a planet candidate, as opposed to an image or detector artifact.

Unified Astronomy Thesaurus concepts: James Webb Space Telescope (2291); Extrasolar gaseous giant planets (509); Exozodiacal dust (500); Coronagraphic imaging (313)

1. Introduction

α Centauri A (α Cen A) is the closest solar-type star to the Sun and offers a unique opportunity for direct imaging with the James Webb Space Telescope (JWST) to detect an exoplanet within its habitable zone (HZ) and to achieve an unprecedented level of sensitivity for the detection of an exozodiacal dust cloud (C. Beichman et al. 2020; A. Sanghi et al. 2025a). Among the nearby stars, α Cen A, primus inter pares, offers a nearly threefold improvement in the angular scale of its HZ and a 7.5-fold boost in the absolute brightness of any planet compared to the next nearest solar-type star, τ Ceti. Specifically, the F1550C coronagraph on board the Mid-Infrared Instrument (MIRI) can be used to probe the 1–3 au ($<4''$) region around α Cen A, which is predicted to be stable within the α Cen AB system for exoplanets and/or an exozodiacal dust cloud (B. Quarles et al. 2018; N. Cuello & M. Sucerquia 2024). The detection of a planet or exozodiacal emission, or more stringent limits on either, would advance our understanding of the formation of planetary systems in binary stellar systems and yield an important target for future observations with both JWST and extremely large ground-based telescopes. Of particular interest is the ability of JWST/MIRI to confirm the detection of a candidate ($C1$) identified using the VISIR mid-infrared camera (10–12.5 μm) on ESO's Very Large Telescope (VLT) as part of the New Earths in Alpha Centauri Region (NEAR) Breakthrough Watch Project (K. Wagner et al. 2021).

In this Letter, we present the results of a deep search for planets and zodiacal dust emission obtained with three epochs of JWST/MIRI coronagraphic imaging observations of α Cen A. This Letter is the first in a series and is followed by A. Sanghi et al. (2025b; hereafter Paper II). It is organized as follows. Section 2 describes the observational strategy and program execution. Section 3 summarizes key aspects of the data processing strategy, the detection of a candidate exoplanet in the 2024 August data, the planet temperature sensitivity of our observations, and upper limits on the presence of exozodiacal emission. Section 4 analyses possible orbital configurations for the candidate planet. The planet's physical properties, as constrained by its observed brightness and orbit, as well as by radial velocity (RV) measurements (R. A. Wittenmyer et al. 2016; L. Zhao et al. 2018), are considered in Section 5. Section 6 discusses the importance of the presence of the candidate planet and the upper limits on exozodiacal emission in the context of theories of planet and disk formation in binary systems, as well as prospects for recovering the candidate in future observations. Finally, Section 7 presents our conclusions. Appendix A provides the complete details of observation preparation and Appendix B includes new Atacama Large Millimeter/submillimeter Array (ALMA) astrometry and an updated ephemeris for the α Cen AB system.

2. Observations

2.1. Observational Strategy

We elected to observe with MIRI and its Four Quadrant Phase Mask (4QPM) coronagraph (G. H. Rieke et al. 2015; G. S. Wright et al. 2015; A. Boccaletti et al. 2022) centered at 15.5 μm (the F1550C filter) for a number of reasons: (1) favorable star–planet contrast ratio for the 200–350 K temperatures expected for a planet heated by α Cen A at 1–3 au; (2) low susceptibility to the effects of wavefront drift at this long wavelength; and (3) the reduced brightness of background objects with typical stellar photospheres. However, despite these advantages, the α Cen AB system presents numerous challenges in planning and executing coronagraphic measurements with JWST at any wavelength.

1. The presence of α Cen B only $7''$–$9''$ away from α Cen A puts the full intensity of this bright, F1550C ~ -0.59 mag star in the focal plane at a position that cannot be attenuated. We developed a strategy (Appendix A.4) to place ϵ Mus at the position α Cen B would occupy (unocculted) during the observation of α Cen A (occulted). This observation would provide a point-spread function (PSF) reference to mitigate the effects of α Cen B.
2. The selection of a reference star is complicated by the requirement that it be both comparably bright to α Cen A and have similar photospheric properties in the F1550C wave band.
3. The moment-by-moment position of α Cen A is the result of a complex interplay of its high proper motion and parallax (as calculated for the location of JWST at the epoch of observation), and of the orbital motions of α Cen A and α Cen B about their common center of mass (see R. Akeson et al. 2021, and Table 1).
4. With F1550C ~ -1.5 mag, α Cen A is too bright for target acquisition (TA) with MIRI, necessitating a blind offset from a nearby star with an accuracy of $<$10 mas to avoid degradation of the coronagraphic contrast (A. Boccaletti et al. 2015). The chosen reference star ϵ Mus (Appendix A.1) is similarly too bright for direct TA, also necessitating a blind offset.
5. Offset stars must be of sufficient astrometric accuracy, be as close as possible to α Cen A or ϵ Mus, but not affected by diffraction or other artifacts from the target stars, and be of sufficient brightness to be readily detectable in a short TA observation at F1000W (Figure 1).
6. The time of observation should minimize the change in the solar aspect angle between the target and reference star observations and thus minimize the change in the telescope's thermal environment.
7. Finally, all MIRI coronagraphic observations using 4QPM are affected by excess background radiation appearing around the quadrant boundaries referred to as "Glow Stick" (A. Boccaletti et al. 2022).

2.2. Planned Observation Sequences

The above considerations led to the observational sequences described below and detailed in Appendix A. Based on in-flight performance, JWST can place both the target and reference star with an accuracy of ∼5–7 mas (1σ, each axis)

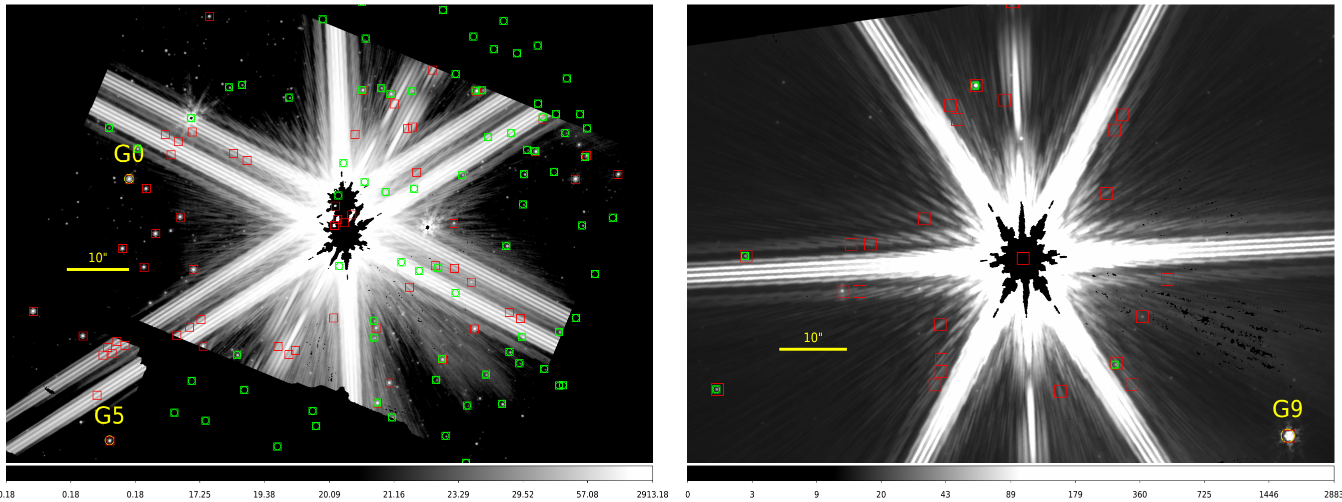

Figure 1. Left: F1000W image of α Cen AB showing Gaia stars (green boxes) and MIRI detections (red boxes). The stars labeled $G0$ and $G5$ were used for TA of α Cen A. Right: similar F1000W image for ϵ Mus. The star labeled $G9$ was used for TA of ϵ Mus.

Table 1
Stellar Properties

Property	α Cen A	α Cen B	ϵ Mus	References
Spectral Type	G2V	K1V	M4III	(1, 2)
Mass ($M_\odot$)	1.0788 ± 0.0029	0.9092 ± 0.0025	...	(3)
Luminosity ($L_\odot$)	1.5059 ± 0.0019	0.4981 ± 0.0007	...	(3)
K (mag)	−1.48 ± 0.05	−0.60 ± 0.05	−1.42 ± 0.05	(2, 4)
F1065C	−1.51 ± 0.05 (160 Jy)	−0.59 ± 0.05 (51 Jy)	−1.9 ± 0.1 (194 Jy)	(5, 6, 7)
F1140C	−1.51 ± 0.05 (120 Jy)	−0.59 ± 0.05 (59 Jy)	−1.9 ± 0.1 (180 Jy)	(5, 6, 7)
F1550C	−1.51 ± 0.05 (63 Jy)	−0.59 ± 0.05 (28 Jy)	−2.0 ± 0.1 (100 Jy)	(5, 6, 7)
Parallax (mas)	750.81 ± 0.38		9.99 ± 0.20	(3, 8)
Distance (pc)	1.33		100	(3, 8)
Proper Motion (μ_α, μ_δ, mas yr^{-1})	(−3639.95 ± 0.42, +700.40 ± 0.17)		(−231.04 ± 0.19, −26.39 ± 0.26)	(3, 8)
R.A.	14:39:26.155	14:39:25.9421	12:17:33.620	(3, 8, 9)
Decl.	−60:49:56.287	−60:49:51.334	−67:57:39.072	(3, 8, 9)

References. (1) J. A. Valenti & D. A. Fischer (2005); (2) J. R. Ducati (2002); (3) R. Akeson et al. (2021); (4) D. Engels et al. (1981); (5) from angular size of α Cen A, $\Theta = 8.502$ mas combined with a Kurucz–Castelli model with $T_{\rm eff} = 5795$ K and log $g = 4.312$ dex (cgs units; P. Kervella et al. 2017); (6) from a fit with a Kurucz model atmosphere using the VOSA spectral energy distribution (SED) utility (D. Engels et al. 1981; J. R. Ducati 2002; F. Castelli & R. L. Kurucz 2003; A. Bayo et al. 2008); (7) F. M. Olnon et al. (1986); (8) Gaia Collaboration et al. (2016); and (9) for ϵ Mus Epoch 2016.0 (Gaia Data Release 3 (DR3)) and for α Cen Epoch 2019.5 (R. Akeson et al. 2021).

behind MIRI/4QPM. To provide diversity in determining the PSF for postprocessing, we selected a nine-point dither pattern for observing the reference star. The multiple reference PSF observations improve the ability of postprocessing algorithms to remove residual stellar speckles and help to mitigate wavefront error (WFE) drifts over the 32 hr duration of the entire sequence. The measurement strategy was as follows.

1. Offset from a Gaia star ($G9$ in Figure 1) to place ϵ Mus at the center of the F1550C coronagraphic mask and make a nine-point dithered set of image observations of the reference star behind MIRI/4QPM. This is followed by observations of a background field to subtract the Glow Stick.
2. Place ϵ Mus at the detector location that α Cen B would occupy in the Roll #1 observation to help mitigate speckles from the unocculted star at the position of α Cen A.
3. Offset from a Gaia star ($G0$ or $G5$ in Figure 1) to place α Cen A at the center of the F1550C coronagraphic mask at the Roll #1 V3 reference axis position angle (PA; V3PA) measured eastward relative to north when projected onto the sky for a sequence of 1250 images, followed by observations of a background field to subtract the Glow Stick.
4. Repeat the α Cen A sequence (#3) at a second V3PA angle (Roll #2).
5. Repeat the ϵ Mus nine-point dither sequence (#1) at the mask center.
6. Repeat the off-axis ϵ Mus observation sequence (#2) but at the detector position of α Cen B in the Roll #2 observation.

2.3. Executed Observation Sequences

The observations of α Cen A (Cycle 1 GO, PID #1618; PI: Beichman, co-PI: Mawet) were initiated in 2023 August, but were unsuccessful due to TA and offset failures. A sequence of short test images was obtained in 2024 June and July to validate the TA strategy. Specifically, in 2024 July, we executed #1 without dithering and #3 with fewer integrations.[22] Following successful execution of the test program, we conducted our full set of science observations in 2024 August. We successfully executed steps #1, #4, and #6 (#2 was not part of the sequence planned for this observation). However, the first roll on α Cen A (#3) and the second ϵ Mus observation (#5) were unsuccessful due to guide star failures.

Based on the results from the 2024 August data, the STScI Director's Office approved a follow-up Director's Discretionary Time (DDT) program (PID #6797; PI: Beichman, co-PI: Sanghi). The complete two roll sequence with associated reference star observations (#1–#6) was attempted in 2025 February as part of this DDT program, but due to a telescope pointing anomaly, the first α Cen A roll (#3) was not executed. All other observations were successful.

The STScI Director's Office approved a second follow-up DDT program (PID #9252; PI: Beichman, co-PI: Sanghi), which resulted in the successful execution of a full two roll sequence in 2025 April. A summary log of all successful observations is provided in Appendix A. In all cases, the accuracy of the offsets from the Gaia stars was consistent with the expected initial pointing accuracy (1σ, 5–7 mas), the offset accuracy (1σ, 1.5 mas), and the line-of-sight jitter (1σ, 1.5 mas) during the observing sequence at each position. The 2025 February Roll #2 and 2025 April Roll #1 observations showed offsets of >10 mas from the 4QPM center or from the ϵ Mus dither pattern and were thus of lower quality (see the dither map in Paper II).

3. Results

3.1. Summary of Data Reduction

Paper II describes in detail the initial pipeline processing, PSF-subtraction techniques for both α Cen A and α Cen B, source identification steps, the photometry and astrometry estimation procedures, and detection sensitivity analysis. Here, we provide a short summary. Level 0 data products were downloaded from MAST, processed for the best up-the-ramp calculation of source brightness and bad pixel rejection (T. D. Brandt 2024; A. Carter et al. 2025), and postprocessed to remove the residual stellar diffraction from α Cen A and α Cen B. We assembled distinct reference PSF libraries for each epoch consisting of the individual 400 frames (per dither position) of each position in the nine-point Small Grid Dither (SGD) pattern of ϵ Mus behind 4QPM and the individual 1250 frames of ϵ Mus at the unocculted position of α Cen B (for a given roll) obtained at the corresponding epoch. We employed reference star differential imaging and jointly subtracted α Cen AB from the 1250 α Cen integrations using the principal-component-analysis-based Karhunen–Loève image processing algorithm (R. Soummer et al. 2012). Signal-to-noise ratio (S/N) maps were generated to search for point sources (D. Mawet et al. 2014) and extended emission (custom method), and assess detection significance.

3.2. Detection of a Point Source around α *Cen A*

A comprehensive search of the $\sim3''$ region around α Cen A revealed a single point-like source in the 2024 August data, $S1$ (Figure 2). The source was detected $\approx1\farcs5$ east of α Cen A at an S/N between four and six (corresponding to a 3.3–4.3σ Gaussian significance for the equivalent false positive probability, see Paper II) with a flux density of $\approx$3.5 mJy (Table 2). The contrast of $S1$ with respect to α Cen A in the F1550C bandpass is $\approx5.5 \times 10^{-5}$. $S1$ is not recovered in the 2025 February and April observations (Figure 2). At wider separations, in all three epochs, we identified two objects denoted KS2 and KS5 that are known from deep 2 μm VLT/NACO imaging to be background stars (P. Kervella et al. 2016). In the 2024 August data, KS2 is seen $\approx6''$ east of α Cen A, after postprocessing, exactly in the position expected for a distant, low proper motion star (Figure 2). The bright object KS5 ($Ks \sim 7$ mag) is detected just off the edge of the coronagraphic field and will eventually pass within a few milliarcseconds of α Cen A (mid-2028; P. Kervella et al. 2016).

Paper II discusses the robustness of the detection of $S1$ and with the help of several tests, presents reasonable evidence that $S1$ is a celestial signal, as opposed to an image artifact. Three primary artifact scenarios are shown to be unlikely.

1. *S1 is not likely a short-lived detector artifact in the* α *Cen AB integrations.* $S1$ was independently detected in multiple subsets of the full 1250 frame integration sequence (Section 4.2.3 in Paper II). Additionally, there was no evidence for transient "hot pixels" in the data, centered on $S1$.
2. *S1 is not likely a PSF-subtraction artifact from the* ϵ *Mus coronagraphic reference images.* $S1$ was detected in postprocessing analyses performed by iteratively excluding each one of the nine dither positions ("leave-one-out" analysis, Section 4.2.4 in Paper II).
3. *S1 is not likely a PSF-subtraction artifact from imperfect subtraction of* α *Cen B.* $S1$ is well matched to the expected PSF profile and behaves differently with respect to changes in the subtraction parameters from another point-like object ($A1$) identified as an artifact from α Cen B. $A1$'s signal disappears both when the number of azimuthal subsections and number of principal components increase. $S1$'s signal persists in both cases (Section 4.2.2 in Paper II).

To assess whether $S1$ is physically associated with α Cen A, we address whether it could be either a background or foreground (solar system) object. Multiple arguments rule out these scenarios.

1. First and most conclusively, the JWST data themselves provide definitive evidence against the hypothesis that $S1$ is a background object. No point-source counterparts to $S1$ are detected at the expected location for a background source in the 2025 February and 2025 April observations (Figure 3). See Paper II for further details.
2. Archival images taken by the Spitzer Space Telescope (Spitzer)/IRAC (G. Rieke & N. Gautier 2004), the Two Micron All-Sky Survey (2MASS), and VLT/NACO (P. Kervella et al. 2016) when α Cen A was up to 1′ away from its current position do not show any sources at the $S1$ position. We also considered the effects of interstellar extinction on background source detectability in archival imaging. Extinction maps from Planck and stellar data along the line of sight toward α Cen provide the range $20 < A_V$ (mag) < 40 (Planck Collaboration et al. 2016;

[22] No ϵ Mus reference star observation was acquired at the detector position of α Cen B in the 2024 July test observations. This severely compromised the quality of the PSF subtraction. Hence, these observations are not presented.

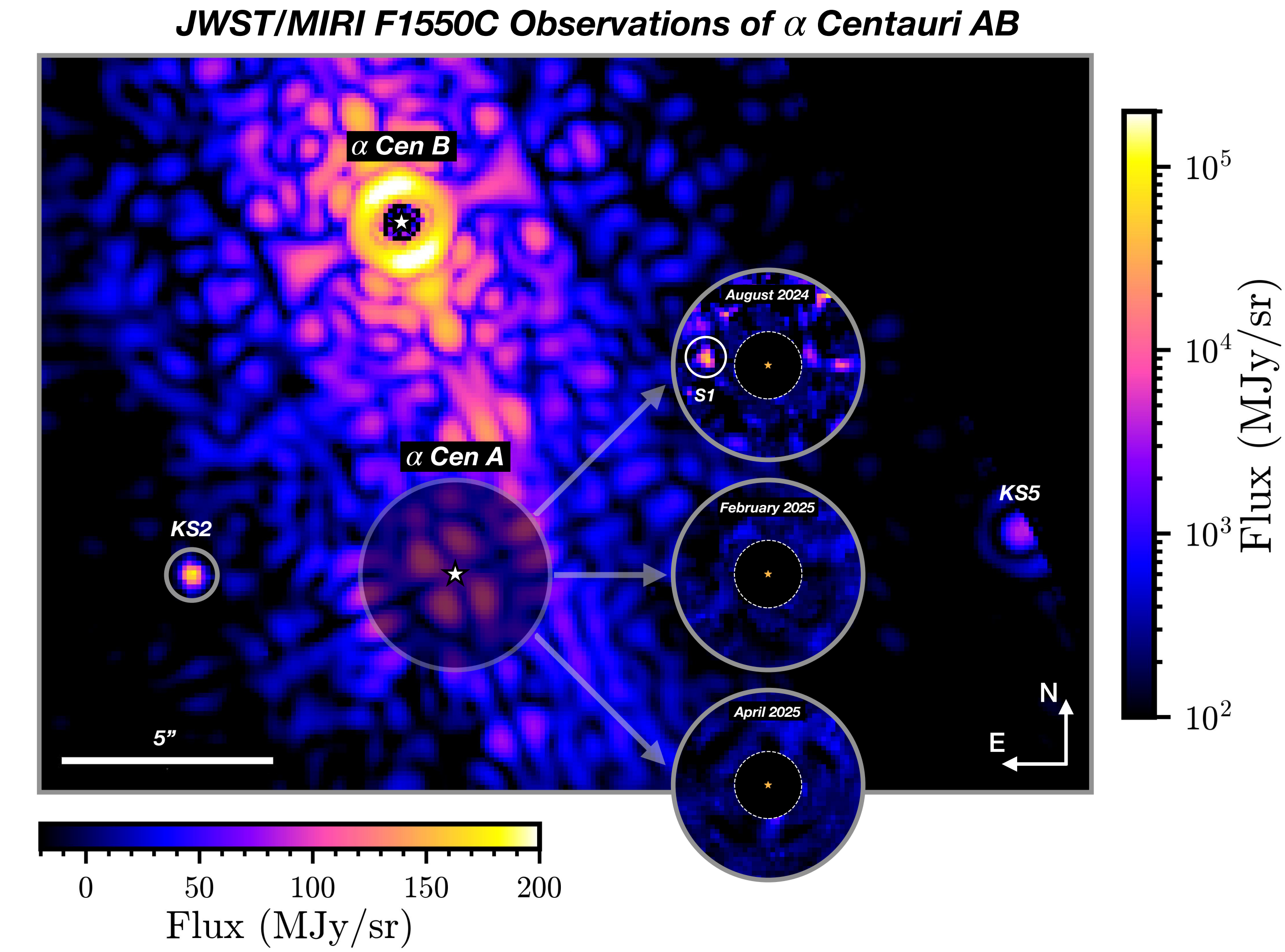

Figure 2. JWST's view of the α Cen AB system. Shown above is a background-subtracted Stage 2b F1550C image of the α Cen AB system from 2024 August. The image is oriented north up and east left. The white stars denote the approximate positions of α Cen B, saturated near the top of the image, and α Cen A in the lower part of the image hidden behind the F1550C mask. The right color bar (logarithmically scaled) is associated with this image. At the edge of the detector, to the west of α Cen A, is the known background source KS5 (P. Kervella et al. 2016). To the east of α Cen A is the known background source KS2 (P. Kervella et al. 2016), shown as an inset, as it is only detected after performing PSF subtraction (no color bar shown for the inset, scaled linearly between -5 and 50 MJy sr^{-1}). An $\approx 2\farcs75$ radius region around α Cen A is shaded and mapped to three PSF-subtracted images, one for each observation epoch. Candidate $S1$ is seen only in 2024 August. The bottom color bar (linearly scaled) is associated with the three PSF-subtracted images. For reference, 1 MJy sr$^{-1} \approx 4.6 \times 10^{-6}$ Jy AiryCore^{-1}, where AiryCore is defined as the area of a circular aperture of diameter = 1 FWHM ($\approx 0\farcs5$).

Table 2
Observations of the Candidate Planet Orbiting α Cen A

ID	Epoch	$(\Delta\alpha, \Delta\delta)$ (arcsec)	(ρ, θ) (arcsec, deg)	Wavelength (μm)	Flux (mJy)	Contrast to α Cen A	S/N
$C1$	2019 Jun 1	$(-0.64, -0.56) \pm 0.05$	$(0.85 \pm 0.05, 228.9 \pm 3.3)$	11.25	1.2 ± 0.4	0.8×10^{-5}	3
$S1$	2024 Aug 10	$(1.50, 0.17) \pm 0.13$	$(1.51 \pm 0.13, 83.5 \pm 4.9)$	15.5	3.5 ± 1.0	5.5×10^{-5}	4–6

Note. Observations of $C1$ were obtained in 2019 by the VLT/NEAR experiment (K. Wagner et al. 2021). PA (θ) is measured east of north.

M. Zhang & J. Kainulainen 2022), making more extreme A_V values unlikely.[23] As shown in Figure 4, if $S1$ were a reddened star (an M0III Kurucz model with $T_{\rm eff} = 3800$ K is shown; R. Buser & R. L. Kurucz 1992) or a normal star-dominated galaxy, its emission would be 4–25 times brighter at IRAC wavelengths than at F1550C and would have been detectable by Spitzer, or in the deep NACO K-band image. This argument applies to any stellar temperature, since at these wavelengths the emission is approximately Rayleigh–Jeans.

3. Figure 4 also shows the SED for a nonphotosphere-dominated galaxy, the prototypical starburst galaxy or ULIRG, Arp 220, at zero redshift (M. Polletta et al. 2007). Such an object could have escaped detection in

[23] Planck Extinction maps: https://irsa.ipac.caltech.edu/data/Planck/release_2/all-sky-maps/maps/component-maps/foregrounds/COM_CompMap_Dust-DL07-AvMaps_2048_R2.00.fits.

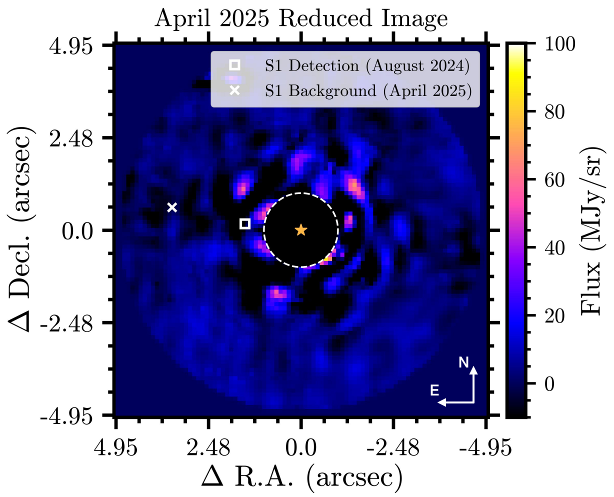

Figure 3. PSF-subtracted image centered on α Cen A for the 2025 April observations, which provides the longest temporal baseline to test the stationary background source hypothesis. A square marks the location where *S*1 was detected in the 2024 August epoch. A cross marks the expected location of *S*1 if it were a fixed background object and showed apparent motion with respect to α Cen A due to the star's parallactic and proper motion. No source is detected at this location.

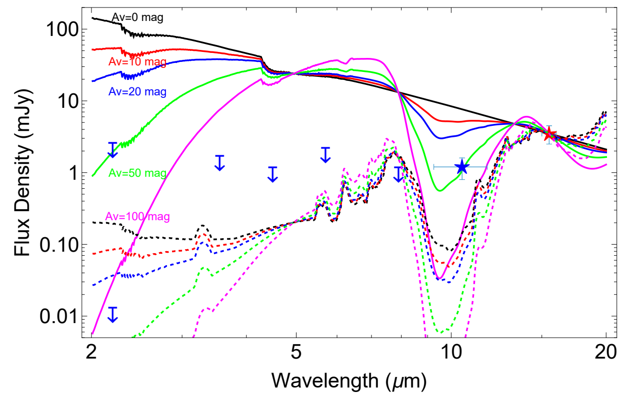

Figure 4. Limits from archival imaging at *S*1's position. The solid, color-coded lines show a photospheric model for an M0III star ($T_{\rm eff}$ = 3800 K) reddened by increasing levels of extinction, all normalized to 3.5 mJy at 15.5 μm (red star). The blue star denotes the flux density of the object denoted *C*1 detected by the VLT/NEAR experiment (K. Wagner et al. 2021). The dashed lines show the SED of a typical starburst galaxy or ULIRG (Arp 220) similarly reddened. Upper limits at the position of *S*1 come from observations at earlier epochs with Spitzer/IRAC (3–8 μm), 2MASS, and NACO (P. Kervella et al. 2016).

the archival data sets, but the probability of chance alignment with an extragalactic background object is extremely low based on source-counting studies in the MIRI broadband filters. M. A. Stone et al. (2024) find that the background density of F_ν(F1500W) $\gtrsim$ 1 mJy sources is $<$0.05 arcmin^{-2}, corresponding to a chance alignment likelihood $< 4 \times 10^{-4}$ within a 3″ field of view.

4. We eliminate the possibility that *S*1 is a foreground solar system object in a number of ways. An inner main belt asteroid (MBA) at 2.2 au with a typical temperature of 200 K would have to have a diameter of $>$2 km to emit $\sim$3 mJy at 15.5 μm. Such objects are extremely rare, $<10^{-4}$ brighter than 3 mJy at 12 μm in a $5' \times 5'$ field at α Cen A's ecliptic latitude of $\beta = -42^\circ$ (T. Y. Brooke 2003). Furthermore, the completeness for such large MBAs is over 90% and the Minor Planet Catalog shows no known objects at the position of α Cen A at the August epoch.[24] Finally, as described in Paper II, there is no angular motion seen between the beginning and the end of the $\sim$2.5 hr MIRI observation compared to the expected $>10''$ hr^{-1} motion for an MBA at the solar elongation of our observations, $\approx$100° (T. Y. Brooke 2003).

Based on all of the above considerations, we pursue the hypothesis that *S*1 is a planet physically associated with and in orbit around α Cen A, as opposed to an artifact or an astrophysical contaminant, and investigate its properties. Given that *S*1 is only detected in a single roll observation in August 2024, we emphasize that it is, at the moment, a planet candidate. Additional sightings of *S*1 are required with JWST, or other upcoming facilities, to confirm what would be "α Cen Ab."

3.3. Planet Detection Limits with JWST/MIRI

We assess our sensitivity to planets around α Cen A across all three epochs of MIRI F1550C observations. Paper II presented the calculation of 2D flux and contrast sensitivity maps. Here, we use the "combined minimum" map from Paper II, which corresponds to the 2D sensitivity map with the best flux sensitivity across all three epochs at each location where the PSF injection–recovery test was performed. We convert the 5σ and S/N = 5 flux sensitivities (see Paper II) to effective temperatures ($T_{\rm eff}$) assuming a blackbody (BB) model and a typical planet radius of 1 $R_{\rm Jup}$ (for smaller planets, the minimum detectable planet $T_{\rm eff}$ increases). The results are shown in Figure 5. The MIRI F1550C observations are sensitive to $T_{\rm eff} \approx 250$ K (1 $R_{\rm Jup}$) planets between 1″ and 2″ for an S/N = 5 detection threshold. Planets colder than 200 K can be detected at wider separations ($>$2″5). We note here that more realistic planet atmosphere models may have a higher brightness temperature (and thus flux) in the F1550C bandpass relative to the effective BB temperature assumed here (see Section 5.2, for example). This would improve the detectability of colder planets at smaller separations than presented here.

3.4. Limits on Extended Emission around α Cen A

C. Beichman et al. (2020) predicted that JWST's ability to resolve the HZ around α Cen A would result in unprecedented sensitivity to warm dust—the analog of the thermal emission from dust generated by collisions the asteroid belt in our solar system. We show below that the current observations have not only met but exceeded those expectations with limits as low as a few times the solar system brightness levels at 15.5 μm.

3.4.1. Exozodi Model Description

As described in Paper II, we injected a number exozodiacal cloud models into the processed α Cen data cubes to set limits on extended "exozodiacal" emission around α Cen A. In the case of α Cen A, stable orbits—and thus significant dust buildup—are limited to within the stable zone, approximately $<$3 au from the star. The solar system zodiacal cloud is therefore a poor proxy for a potential exozodi around α Cen A. For a more realistic representation, we consider the scenario of an asteroid belt analog (ABA) located between 2 and 3 au, where dust is produced in collisions, which is then transported

[24] https://minorplanetcenter.net/cgi-bin/checkmp.cgi

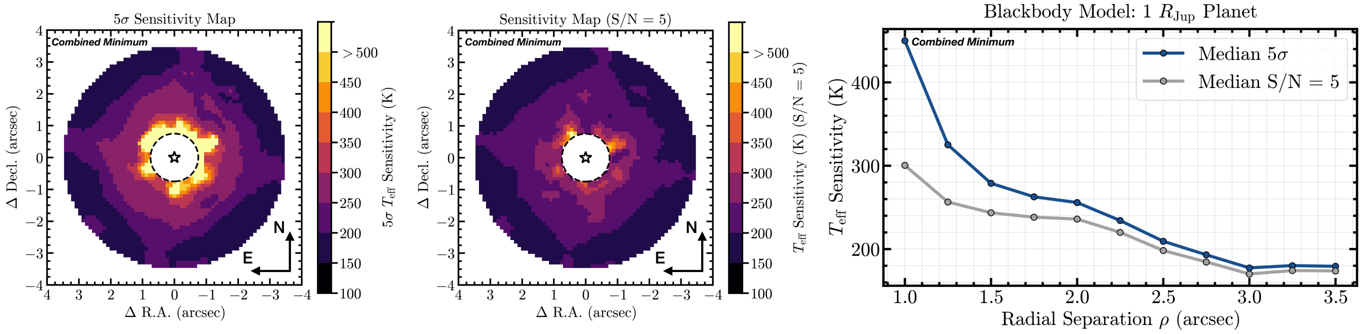

Figure 5. Left: 2D 5σ planet effective BB temperature sensitivity map, combined across all epochs by selecting the best sensitivity ("combined minimum," see Paper II), in sky coordinates (north up, east left). The central region (<0″75, or <1.5 FWHM, radial separations) is masked (poor detectability). A discrete color map is chosen to highlight the different sensitivity zones across the image. Center: same as the left panel but for an S/N = 5 detection threshold. Right: 5σ and S/N = 5 median planet effective BB temperature curves combined across all epochs.

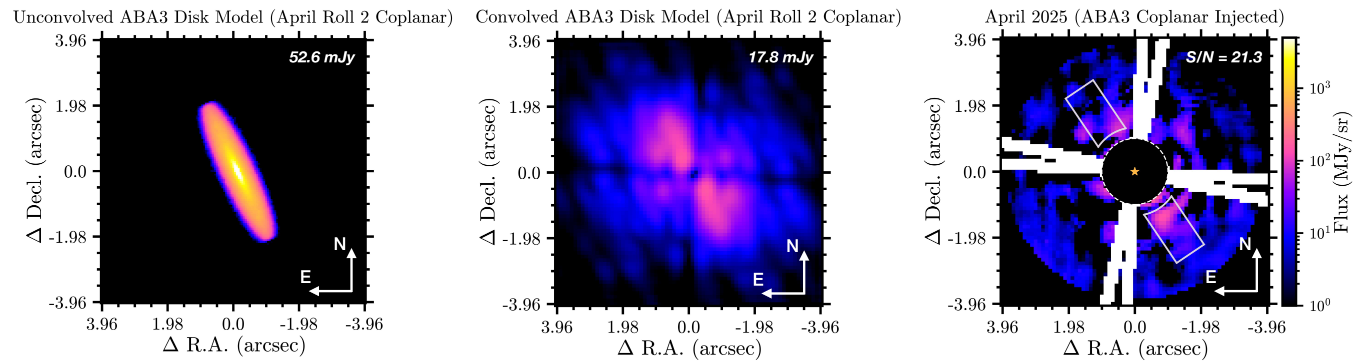

Figure 6. Left: unconvolved ABA-3 exozodi model coplanar with the α Cen AB binary. Center: the exozodi model in the left panel after PSF convolution (for the 2025 April observation orientation). Right: PSF-subtracted image showing the recovery of the ABA-3 exozodi model injected in the raw α Cen AB data set from the 2025 April observations. The regions of the image affected by the MIRI/4QPM transition boundaries at each roll are masked. The aperture that yielded the highest S/N (=21.3) detection for the injected disk is shown (see Paper II for details). All images are plotted on a common logarithmic color scale.

inward under Poynting–Robertson (PR) drag. This scenario is captured by the semianalytical model of J. K. Rigley & M. C. Wyatt (2020), which combines approaches to determine (1) the size distribution arising in a planetesimal belt under collisions and PR drag loss (M. C. Wyatt et al. 2011), and (2) how it evolves interior to the belt under further collisional and drag-induced evolution (M. C. Wyatt 2005). The resulting optical depth distribution (across grain sizes and disk radii) is then combined with the particles' thermal emission properties, determined using Mie theory, to compute the disk's surface brightness distribution.

Following the approach of M. Sommer et al. (2025), we generate astrophysical scenes of the inclined, edge-on disks from the respective surface brightness profiles, and convolve them with the spatially varying PSF of the F1550C coronagraphic filter (modeled using `STPSF`; M. D. Perrin et al. 2014), before injecting them into the MIRI data cubes. An example of an exozodi scene, before and after PSF convolution, alongside a PSF-subtracted image obtained after model injection, is shown in Figure 6. Note that all exozodiacal disks considered here are assumed to be coplanar with the α Cen AB plane, which is a reasonable assumption for potential circumstellar debris disks in binaries (see Section 6.2.1), although the invariable plane about which the orbit precesses could also be affected by the gravity of massive planets in the system.

For the model parameters, we further assume a belt opening angle of 5°, a size-independent catastrophic disruption threshold of 10^7 erg g^{-1} (representing the grains' collisional strength), as well as a grain composition of one-thirds amorphous silicates and two-thirds organic refractories by volume, which determines their Mie-theory-derived optical properties. Four models of different belt dust masses, ABA-1 to ABA-4, are considered, for which the derived quantities are summarized in Table 3, including the mass compared to our own Main Asteroid Belt (MAB). The resulting surface brightness profiles of the different models are compared in Figure 7. Here, the ABA-1 model differs from the other models in having a sharper decline of surface brightness at the inner belt edge. This is because, at that mass, even small dust is effectively ground down to blowout sizes before it can migrate inward past the belt. As a result, further increases in belt mass only enhance the local brightness within the belt, while the interior regions reach saturation (M. C. Wyatt 2005).

To give an indication of the plausibility of the ABA models, we also conduct a simplified analysis of the total belt mass and collisional lifetimes within the belt, assuming a canonical collisional cascade with a size distribution following a power-law slope of −3.5 (J. S. Dohnanyi 1969) extending up to a maximum planetesimal size of 1000 km. Comparing the collisional lifetime of the largest planetesimal to the system age of α Cen (∼5 Gyr) shows that the ABA-1 model is likely not viable, since even with planetesimals as large as 1000 km, collisions would have inevitably eroded the planetesimal belt to below the ABA-1 level over the system's age. In contrast, ABA-2 is marginally consistent with the anticipated level of

Table 3
Exozodiacal Disk Models

Model	$M_{\rm dust}$ ($10^{-8}\,M_\oplus$)	$M_{\rm belt}$ ($M_{\rm MAB}$)	$T_{\rm coll,1000\ km}$ (Gyr)	$F_{\rm d,15}$ (mJy)	$F_{\rm d,15}/F_{\star,15}$ $\times 10^{-4}$	$\frac{F_{\rm d,24}}{\sigma_{24}}$a	$\frac{F_{\rm d,70}}{\sigma_{70}}$	$\frac{F_{\rm d,100}}{\sigma_{100}}$	$L_{\rm d}/L_\star$ $\times 10^{-7}$	Z_L	Z_Σ	S/N
ABA-1	20	28	0.88	596	69	1.04	0.29	0.76	94	58	84	78.7
ABA-2	4	5.6	4.40	156	18	0.27	0.07	0.17	27	17	29	52.6
ABA-3	2	2.8	8.80	53	6.1	0.09	0.04	0.09	8.3	5.1	8.4	21.3
ABA-4	1.2	1.7	14.5	20	2.3	0.03	0.02	0.06	3.0	1.8	3.0	5.8
1-zodi	⋯	⋯	⋯	8.8	1.0	0.02	0.02	0.06	1.5	0.94	1.0	−0.7

Note. Exozodi models used for injection and derived quantities. Columns: $M_{\rm dust}$, the ABA model dust mass parameter (belt mass up to 1 cm grain size); $M_{\rm belt}$, the ABA model belt mass up to the largest planetesimal (1000 km) in units of the solar system main asteroid belt ($M_{\rm MAB} = 4 \times 10^{-4}\,M_\oplus$); $T_{\rm coll,1000\ km}$, the collisional lifetime of the largest planetesimal; $F_{\rm d,15}$, the total disk flux at 15.5 μm; $F_{\rm d,15}/F_{\star,15}$, the fractional disk flux at 15.5 μm; $\frac{F_{\rm d,24}}{\sigma_{24}}$, photometric significance for MIPS24; $\frac{F_{\rm d,70}}{\sigma_{70}}$, photometric significance for PACS70; $\frac{F_{\rm d,100}}{\sigma_{100}}$, photometric significance for PACS100 (all uncertainties from J. Wiegert et al. 2014); $L_{\rm d}/L_\star$, the fractional disk luminosity; Z_L, the zodi level by fractional luminosity; Z_Σ, zodi level by Earth-equivalent insolation distance (EEID) surface density; and S/Ns of injection–recovery tests with the 2025 April data set for the case of binary coplanar disks.

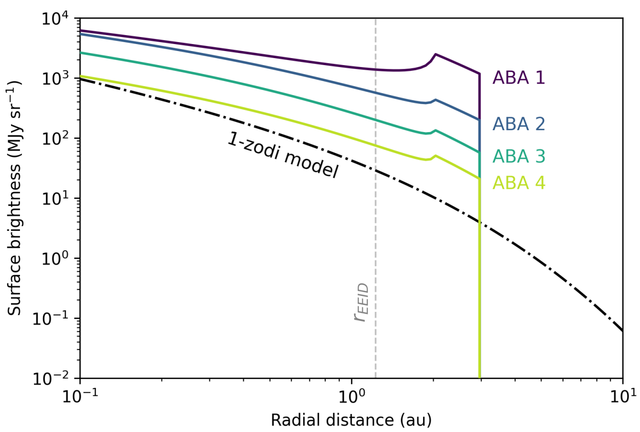

Figure 7. Surface brightness distribution of injected zodi models. ABA-scenario zodis for different belt masses are represented by solid lines. Our fiducial 1-zodi model based on the T. Kelsall et al. (1998) model is represented by the dashed–dotted line.

erosion, while ABA-3 and ABA-4 are more readily compatible with the system's age, only requiring planetesimal masses of a few times that of the solar system's main asteroid belt. Nevertheless, we retain the ABA-1 model in this analysis for comparison purposes.

For reference, we also include an exozodi model that is similar to the solar system zodi, even though its radial extent is nonphysical around α Cen A. This fiducial "1-zodi" model is derived from the T. Kelsall et al. (1998) geometrical model for the solar system's dust cloud, which was fitted to infrared zodiacal light observations by COBE/DIRBE. Here we use the radial surface density distribution approximation derived by G. M. Kennedy et al. (2015) for the T. Kelsall et al. (1998) model. Using the emissivities fitted by T. Kelsall et al. (1998), we calculate the disk's corresponding surface brightness distribution at 15.5 μm, which is also shown in Figure 7. We then use the same image synthesis pipeline as with our ABA exozodi models, the result of which closely matches the outcome of applying the `zodipic` model—an IDL implementation of the T. Kelsall et al. (1998) model (M. Kuchner 2012)—around α Cen A (see C. Beichman et al. 2020), and likewise inject this 1-zodi model into the MIRI data cubes.

While our ABA exozodi models are not strictly comparable to the solar system's zodiacal cloud in terms of geometry, it is still useful to define a "zodi level" that quantifies the dust content of the disks relative to the solar system. Two wavelength-independent metrics for this are the total disk luminosity and the surface density within the HZ. The luminosity-based zodi level is defined as the ratio of the exozodi's fractional luminosity to that of the solar system's zodiacal cloud:

$$Z_L = \frac{L_{\rm d}}{L_\star} \Bigg/ \frac{L_{\rm d,SS}}{L_\odot}, \tag{1}$$

while the surface-density-based zodi level is given by the ratio of the disk surface density at the EEID, $r_0 = \sqrt{L_\star/L_\odot}$ au—approximately 1.23 au for α Cen A—to that of the solar system at 1 au ($\Sigma_{0,\rm SS}$):

$$Z_\Sigma = \frac{\Sigma_0}{\Sigma_{0,\rm SS}}, \tag{2}$$

with $\Sigma_{0,\rm SS} = 7.12 \times 10^{-8}$ (G. M. Kennedy et al. 2015). As discussed by G. M. Kennedy et al. (2015), Z_Σ serves as a proxy for the exozodi's surface brightness in the HZ and is therefore useful for assessing its impact on direct imaging of Earth-like planets. Both definitions of the zodi level are provided in Table 3 for our set of models.

3.4.2. Comparison with Previous Exozodi Searches

The results of the injection–recovery analysis of our various exozodi models, presented in Paper II, are summarized by the corresponding S/N values in Table 3. We find that the three brightest injected exozodi models (ABA-1 to ABA-3) are reliably recovered by our method at S/N $\gtrsim$ 20. The measured S/N for the faintest model, ABA-4, is ∼6. However, this S/N level does not constitute a reliable detection as it is consistent with the range of S/Ns measured in the original image, when no disk model is injected (see Paper II). At the low flux level of ABA-4, the image is dominated by PSF-subtraction artifacts from α Cen B or the 4QPM transition boundaries. In summary, these observations are sensitive to emission from an exozodiacal cloud that is coplanar with the binary orbit at a level of $Z_L \approx 5$ or $Z_\Sigma \approx 8$. This represents an unprecedented sensitivity compared with previous observations and is facilitated by the system's proximity and the model disks' near-edge-on orientation, which our recovery method is tailored to (see Paper II).

It is first worth acknowledging that previous photometric searches have not detected significant excess dust emission at any wavelength (J. Wiegert et al. 2014; B. Yelverton et al. 2019). While J. Wiegert et al. (2014) suggest a Spitzer/MIPS excess at 24 μm at 2.5σ, even our brightest model disk, ABA-1, yields an excess at 24 μm of only around 1σ (see Table 3). Since the ABA-1 model would have easily been detected by our observations, we can confidently rule out the presence of a static (inclined) exozodi to have caused the reported feature. Excesses of our model disks in the far-infrared for Herschel PACS70 and PACS100 observations are of even lower significance, consistent with previous nondetections. This means that any circumstellar disk would have to be even more massive than ABA-1 to have shown up in previous mid- and far-infrared photometric observations, indicating that our observations which could detect ABA-3 are at least 10 times more sensitive in terms of the belt's dust mass.

This improvement in sensitivity arises because photometric observations do not provide the most stringent limits on the presence of dust, due to calibration uncertainties that limit detectable excesses to typically more the 10% of the stellar flux (C. A. Beichman et al. 2005), but with sensitivity approaching 2% in recent studies with JWST (J. Farihi et al. 2025). By that metric it is clear that our resolved imaging approach is able to improve on that limit by about 2 orders of magnitude, since we were able to successfully suppress the stellar emission to recover the signal of the ABA-3 model, which has an excess of ∼0.06% at 15.5 μm (see Table 3). In principle, lower dust levels than obtained via simple photometry can be achieved using nulling interferometry to suppress the stellar emission. The largest and deepest survey of this kind was the HOSTS survey, which used the Large Binocular Telescope (LBT) interferometer to search for exozodi emission in the HZ at 11 μm. While α Cen A was not included in that survey, due to its Southern Hemisphere location and its binarity, the survey results show that the best 1σ sensitivities achieved for (single) solar-type stars reached as low as 0.05% on the null depth, which corresponds to a limit of ∼0.3% for the total flux required for a detection (S. Ertel et al. 2018, 2020). That is, our imaging observations achieved a limit at least 5 times lower than is achievable with nulling interferometry. A similar conclusion is reached by comparing the 5–8 zodi levels of the ABA-3 model (see Table 3) with the best reported zodi limits from the HOSTS survey of ∼70 zodis. This is similar to the sensitivity level of previous mid-infrared coronagraphic imaging of α Cen A with VLT/VISIR, since K. Wagner et al. (2021) reported a resolved source ($C1$) that could be fitted with an ∼60 zodi (3σ) exozodi model. Such a disk would be in between our ABA-1 and ABA-2 models, and thus would have been easily detected by our observations. The VLT/VISIR noise level is 5–10 times higher than JWST's. We can thus rule out that $C1$ belongs to a static clump of exozodi material at this level. The comparisons with previous observations demonstrate the dramatic improvement in sensitivity achieved by the JWST measurements.

4. Orbital Modeling of $S1 + C1$

With only a single JWST/MIRI sighting (and nondetections at two other epochs), it is challenging to uniquely constrain the orbit of $S1$. To make progress, we consider the family of orbits that (a) fit the relative astrometry of $S1$ and the VLT/NEAR 11.25 μm candidate $C1$ (K. Wagner et al. 2021), which we treat as an earlier detection of the $S1$ object (and in this context, is referred to as the $S1 + C1$ candidate); (b) are dynamically stable in the presence of α Cen B; and (c) are consistent with the nondetection of $S1 + C1$ in the 2025 February and April observation epochs. Additionally, we consider the consistency of the candidate's orbits with existing RV upper limits.

4.1. Selection of Stable Orbits

First, we randomly generate 10^7 orbits matching the astrometry of $S1$ and $C1$ (Table 2) using the Orbits For The Impatient algorithm via the `orbitize!` package (S. Blunt et al. 2017, 2020). We apply the default priors in the `orbitize!` code to the candidate planet's orbital elements and use Gaussian priors for α Cen A's mass and parallax ($M_A = 1.0788 \pm 0.0029$ $M_\odot$, $\pi = 750.81 \pm 0.38$ mas; R. Akeson et al. 2021). Next, we evaluate the stability of the accepted orbits using the N-body simulation software `Rebound` (H. Rein & S.-F. Liu 2012) over million-year timescales using the `WHFAST` integrator (H. Rein et al. 2019). A given simulation is deemed unstable for very high planetary eccentricity ($e_p > 0.95$) or large planetary distances from the host star ($d_p > 5$ au). Previous studies showed that orbits that meet either criterion are very likely to be unstable on billion-year timescales (B. Quarles & J. J. Lissauer 2016, 2018), where more than 90% of orbits stable on a million-year timescale were also stable for billion-year timescales. We find that 30% of the orbits from the initial `orbitize!` sample are dynamically stable.

4.2. Incorporating Constraints from Nondetections

We investigate which of the above $S1 + C1$ stable orbits are consistent with nondetections in the 2025 February and April observation epochs using the 2D sensitivity maps generated for both epochs in Paper II. Specifically, we use the S/N = 5 sensitivity map (rather than the 5σ significance sensitivity map) to be stricter in eliminating orbits where $S1 + C1$ would have been marginally recovered in our follow-up observations. The sensitivity maps provide the minimum point-source flux detectable at an S/N = 5 at different sky coordinates around α Cen A. For each of the stable orbits above, we predict the sky position of the candidate planet in the 2025 February and April observations, and check the corresponding location in the sensitivity map to evaluate whether it would have been detected (for a flux of 3.5 mJy). Orbits where the candidate would have been recovered in either of the two epochs are eliminated. We find that 52% of the stable orbits that fit the S1 + C1 astrometry are also consistent with nondetections in both 2025 February and April (Figure 8). There is, thus, an a priori significant chance that, if real, the planet candidate could have been missed in both follow-up observation epochs.

The posteriors for the three key orbital elements (semimajor axis a, eccentricity e, and mutual inclination $i_{\rm mutual}$ with respect to the α Cen AB binary orbit)[25] of the stable orbits consistent with the nondetections (Figure 9) show that there are four families of orbits.[26] They correspond to the number of orbital periods that have elapsed between the VLT/NEAR

[25] The mutual inclination is calculated using Equation (19) in J. W. Xuan & M. C. Wyatt (2020) and using the orbital parameters for α Cen AB in R. Akeson et al. (2021).

[26] We do not consider the small fraction (∼0.2% of the total number) of $a < 1.5$ au orbits in Figure 9 as they do not agree with $S1$'s relative astrometry within the 1σ uncertainties.

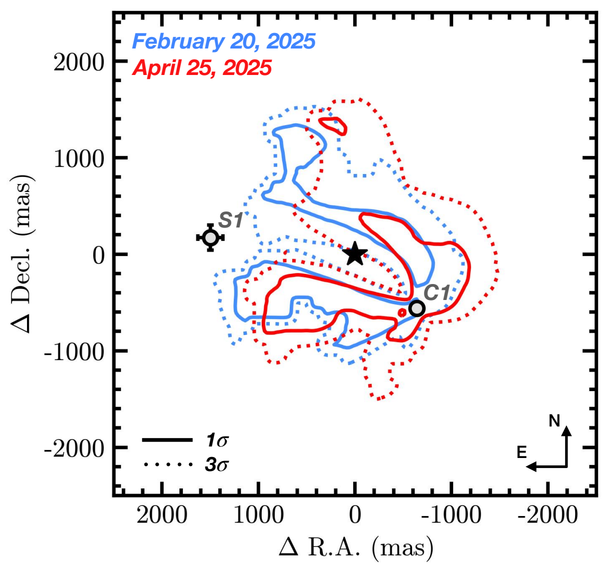

Figure 8. 1σ (solid) and 3σ (dotted) contours showing the sky-projected positions of the $S1 + C1$ candidate consistent with a nondetection in the 2025 February (blue) and April (red) observation epochs.

observations in 2019 June and the JWST detection in 2024 August (either ∼1.5 or ∼2.5 periods, for $a \approx 1.6$ au and $a \approx 2.1$ au, respectively) and orbits in either the prograde ($i_{\rm mutual} \approx 50°$) or retrograde ($i_{\rm mutual} \approx 130°$) direction (Figure 10). In addition to being significantly inclined, the $S1 + C1$ planet candidate is in a moderately eccentric (≈0.4) orbit. A summary of the mean orbital parameters for each family (no RV constraint case) is provided in Table 4. Note that all orbits presented are dynamically stable as evaluated previously (Section 4.1).

4.3. Consistency with Radial Velocity Limits

To the family of stable orbits consistent with the nondetections, we can add a constraint of $K_{\rm RV} < 3$ m s^{-1} (1σ; R. P. Butler et al. 2004; L. Zhao et al. 2018) on the RV of α Cen A, which is also observed in the HARPS RV residuals (P. Kervella et al. 2025, in preparation). This systematic noise floor constrains the minimum mass ($M_{\rm p} \sin i$) of any planet around α Cen A to be $<100\ M_\oplus$ (2σ) or $<150\ M_\oplus$ (3σ) within ≈2 au. Among the dynamically stable $S1 + C1$ orbits consistent with the nondetections, assuming $M_{\rm p} = 100\ M_\oplus$, we find that 4% of these orbits result in $K_{\rm RV} \leqslant 3$ m s^{-1}, 50% result in $K_{\rm RV} \leqslant 6$ m s^{-1}, and 99.8% of all orbits result in $K_{\rm RV} \leqslant 9$ m s^{-1} (Figure 11, the maximum $K_{\rm RV}$ is ≈11 m s^{-1}). Table 4 presents the orbital parameters for each case. The semimajor axis and eccentricity remain largely unchanged after applying the RV constraints; however, the mutual and sky inclinations vary as the RV constraint becomes stricter (smaller reflex motion). In summary, the astrometric positions of $S1 + C1$ can be fit by dynamically stable orbits consistent with both the nondetections in the follow-up observations and existing RV limits. All dynamically stable $S1 + C1$ orbits consistent with the nondetections can be retrieved from doi: 10.5281/zenodo.16280658.

5. Photometric Modeling of $S1 + C1$

In this section, we consider the available photometric data points for the α Cen A planet candidate (JWST/MIRI 15.5 μm and possibly VLT/NEAR 11.25 μm) to investigate its bulk physical properties. While the photometric data are sparse at the moment, there are some physical constraints that can be applied to aid modeling efforts. First, the effective temperature of the planet candidate is expected to be set by heating from α Cen A. Second, the radius of a mature (∼5 Gyr) gas giant planet cannot significantly exceed 1–1.2 $R_{\rm Jup}$ (allowing for some variations if the planet is rapidly rotating and viewed pole on, for example) unless it is located in a very tight "hot Jupiter" orbit, which is not the case as seen in the previous section on orbital modeling. Finally, the mass of the planet must be consistent with the limits set by the RV measurements (L. Zhao et al. 2018). Subject to these constraints, we examine a range of plausible atmospheric models as well as thermal emission from a Saturn-like particle ring to explain the photometric data.

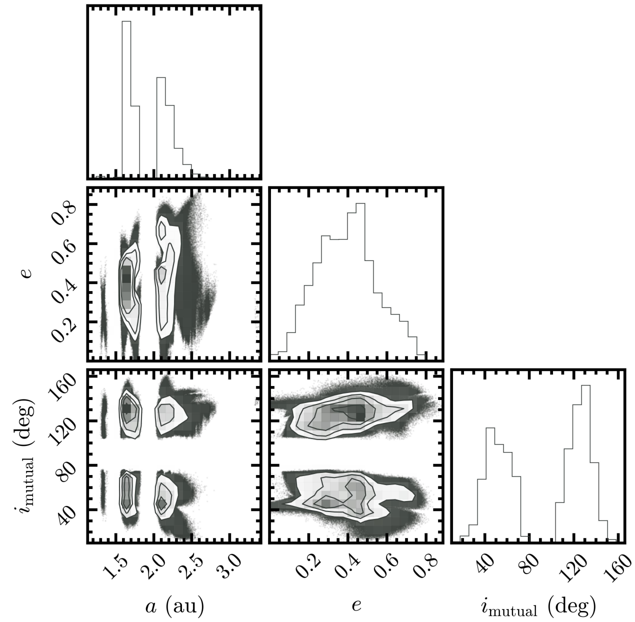

Figure 9. Key parameters for stable planetary orbits fitting the $S1 + C1$ astrometry and consistent with the 2025 February and April nondetections. Four orbital families are observed (prograde, retrograde, $a > 2$ au, and $a < 2$ au).

5.1. Equilibrium Temperature

We use the orbital information to infer the range of plausible effective temperatures for the planet candidate, heated by α Cen A. The equilibrium temperature for a planet on an eccentric orbit depends on the instantaneous stellar input, the planet's thermal inertia, and radiative timescale. For a gas giant planet, any variations of temperature through the orbit are damped by the thermal inertia of the dense H–He atmosphere (A. Quirrenbach 2022). In such a scenario, the correction to the equilibrium temperature to account for changes in the insolation averaged over an eccentric orbit are small, only a few percent, for eccentricities up to 0.5 (R. G. Johnson & B. T. McClure 1976; A. Quirrenbach 2022). The flux-averaged temperature of a body heated by and orbiting α Cen A in an eccentric orbit, $T_{\rm eq}$, at a distance d is given by

$$T_{\rm eq} = T_\star \cdot \left(\frac{1 - A_B}{4f}\right)^{1/4} \cdot \sqrt{\frac{R_\star}{d}} \cdot (1 - e^2)^{-1/8}, \quad (3)$$

where $T_\star = 5766$ K (L. Zhao et al. 2018), $R_\star = 1.2175\ R_\odot$ (R. Akeson et al. 2021), A_B is the Bond albedo, and full heat

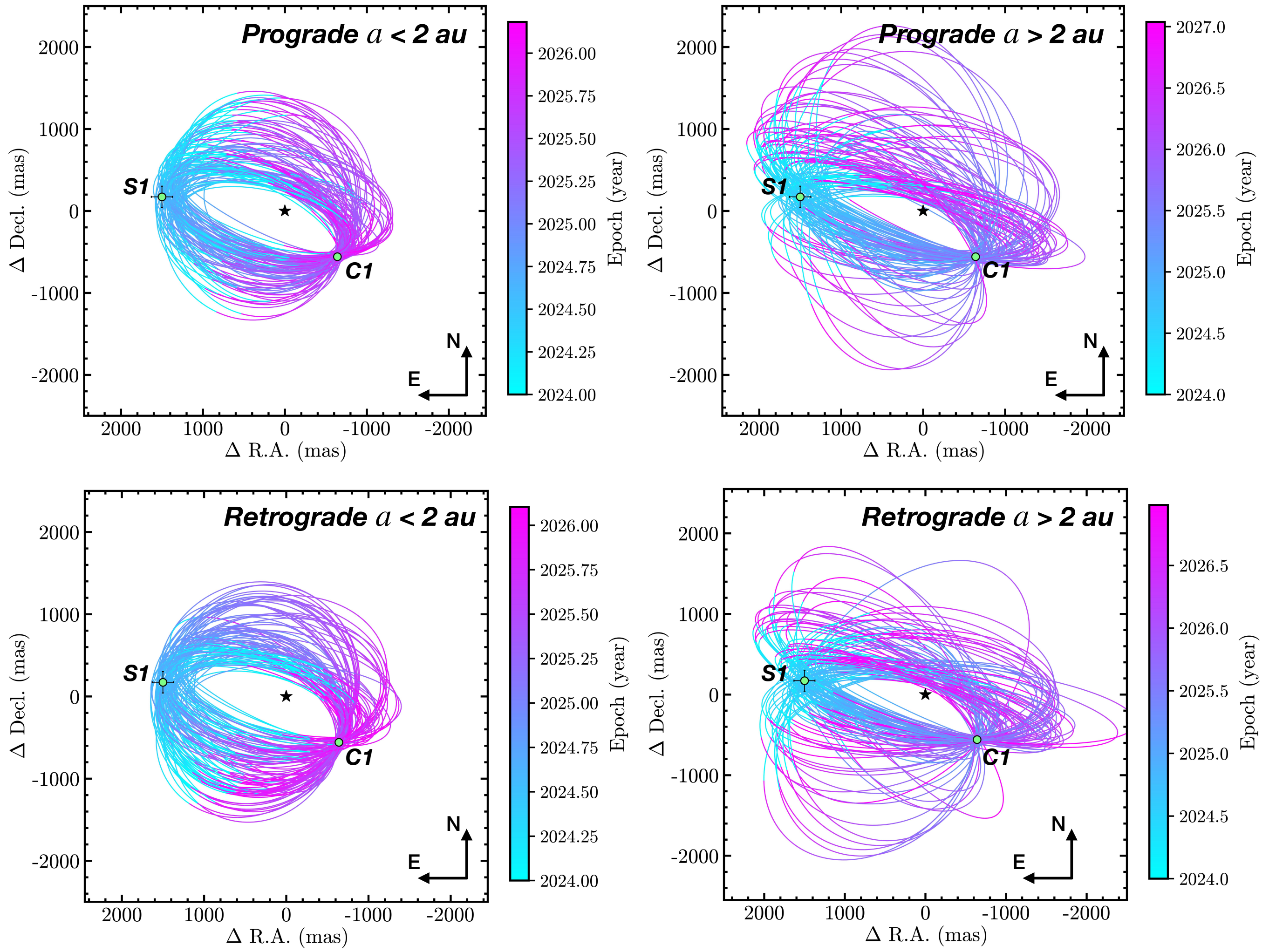

Figure 10. 100 randomly selected stable planetary orbits fitting the $S1 + C1$ astrometry (marked as green points) and consistent with the 2025 February and April nondetections, for each orbital family.

redistribution ($f = 1$) is assumed. Adopting $A_B = 0.3$ (intermediate between the values for most hot Jupiters and those of the solar system gas giants), we compute $T_{\rm eq}$ for all $S1 + C1$ stable orbits consistent with the nondetections (Section 4) and find a bimodal distribution with peaks at ≈195 K and ≈220 K (Figure 12). The lower temperatures correspond to orbits in the $a > 2$ au families and the higher temperatures correspond to orbits in the $a < 2$ au families (Table 4).

The contributions of additional sources of heat for the planet candidate's temperature are negligible compared to stellar insolation. (1) *Residual heat of formation*. α Cen A is ∼5 Gyr old. For a similar internal radiation flux (F) as Jupiter or Saturn, $T_{\rm int} <$ 110 K (L. Li et al. 2018), the increase in temperature is negligible, due to $T \propto F^{1/4}$ and the planet candidate's higher expected $T_{\rm eq}$. (2) *Radiation from α Cen B*. α Cen B is less luminous than α Cen A by a factor of ∼3 (R. Akeson et al. 2021) and at the time of JWST observations was ∼20 au away from α Cen A. Thus, its contribution to heating is negligible. (3) *Tidal heating*. The $S1 + C1$ candidate is in an eccentric orbit. However, $\dot{E}_{\rm tide} \propto a^{-15/2}$ (S. J. Peale & P. Cassen 1978) is negligible for $a \sim 2$ au. (4) *Heating from radioactivity*. This is negligible for Neptune, which is both much colder than $S1 + C1$ and likely has a larger fraction of radioactive isotopes.

5.2. Planet Atmospheric Models

The goal in this section is to obtain first estimates of the planet candidate's fundamental parameters ($T_{\rm eff}$, radius, and mass) using atmospheric model grids available in the literature for cold planets and brown dwarfs. Given the numerous atmospheric parameter degeneracies involved in fitting two photometric data points, particularly in the observationally unexplored low-mass ($\lesssim$200 $M_\oplus$), low temperature (<300 K) planetary regime (see for example, K. A. Crotts et al. 2025), we aim only to provide example scenarios that can explain the observed flux measurements. Detailed atmospheric modeling is appropriate for future studies when additional photometry and/or spectroscopy is available (see Section 6.3).

We jointly fit the F1550C JWST/MIRI flux and the 11.25 μm VLT/NEAR flux (Table 2), assuming they are related (as indicated by the orbital fits in the previous section). The fitting procedure synthesizes model photometry in the F1550C bandpass (≈15.15–15.85 μm, using the transmission curve from the Spanish Virtual Observatory (SVO) filter profile service)[27] and the VLT/NEAR bandpass (≈10–12.5 μm, constant transmission assumed), and finds the minimum radius (<1.2 $R_{\rm Jup}$) that

[27] http://svo2.cab.inta-csic.es/theory/fps/

Table 4
Key $S1 + C1$ Orbital Parameters

Sightings Used	Orbit Type	a (au)	e	i_{mutual}[a] (deg)	i_{sky}[b] (deg)	T_{eq}[c] (K)
$S1$, $C1$, and ND[d]	Prograde, $a < 2$ au No RV constraint	1.66 ± 0.06	0.37 ± 0.12	54 ± 11	55 ± 15 or 124 ± 13	223 ± 5
$S1$, $C1$, and ND	Prograde, $a < 2$ au $K_{\mathrm{RV}} < 6$ m s^{-1}	1.64 ± 0.07	0.33 ± 0.10	58 ± 11	41 ± 13 or 136 ± 9	223 ± 5
$S1$, $C1$, and ND	Prograde, $a < 2$ au $K_{\mathrm{RV}} < 3$ m s^{-1}	1.58 ± 0.08	0.27 ± 0.04	70 ± 4	16 ± 5	225 ± 6
$S1$, $C1$, and ND	Prograde, $a > 2$ au No RV constraint	2.18 ± 0.09	0.43 ± 0.18	49 ± 12	78 ± 26	197 ± 6
$S1$, $C1$, and ND	Prograde, $a > 2$ au $K_{\mathrm{RV}} < 6$ m s^{-1}	2.14 ± 0.07	0.33 ± 0.14	51 ± 11	68 ± 27	195 ± 5
$S1$, $C1$, and ND	Prograde, $a > 2$ au $K_{\mathrm{RV}} < 3$ m s^{-1}	2.09 ± 0.02	0.46 ± 0.03	64 ± 6	22 ± 4	200 ± 1
$S1$, $C1$, and ND	Retrograde, $a < 2$ au No RV constraint	1.68 ± 0.06	0.36 ± 0.12	126 ± 10	64 ± 7 or 132 ± 19	221 ± 6
$S1$, $C1$, and ND	Retrograde, $a < 2$ au $K_{\mathrm{RV}} < 6$ m s^{-1}	1.67 ± 0.08	0.34 ± 0.10	123 ± 11	49 ± 6 or 144 ± 14	221 ± 6
$S1$, $C1$, and ND	Retrograde, $a < 2$ au $K_{\mathrm{RV}} < 3$ m s^{-1}	1.65 ± 0.08	0.36 ± 0.07	115 ± 5	162 ± 5	223 ± 6
$S1$, $C1$, and ND	Retrograde, $a > 2$ au No RV Constraint	2.23 ± 0.14	0.43 ± 0.18	126 ± 10	89 ± 24	194 ± 8
$S1$, $C1$, and ND	Retrograde, $a > 2$ au $K_{\mathrm{RV}} < 6$ m s^{-1}	2.23 ± 0.16	0.32 ± 0.14	122 ± 9	88 ± 29	192 ± 8
$S1$, $C1$, and ND	Retrograde, $a > 2$ au $K_{\mathrm{RV}} < 3$ m s^{-1}	2.09 ± 0.02	0.64 ± 0.03	115 ± 5	163 ± 5	208 ± 3

Notes. Parameters are reported as mean ± standard deviation. K_{RV} assumes a planet mass of 100 $M_\oplus$.
[a] Inclination relative to the α Cen AB orbital plane ($i_{\mathrm{AB}} = 79.^{\circ}2430 \pm 0.^{\circ}0089$, $\Omega_{\mathrm{AB}} = 205.^{\circ}073 \pm 0.^{\circ}025$ from R. Akeson et al. 2021).
[b] Inclination relative to the plane of the sky. Bimodal distributions (about $i_{\mathrm{sky}} = 90°$) are presented as two sets of values.
[c] Flux-averaged mean planet temperature for $A_B = 0.3$ (see Section 5.1)
[d] "ND" denotes that orbits were checked for consistency with nondetections in the 2025 February and April epochs.

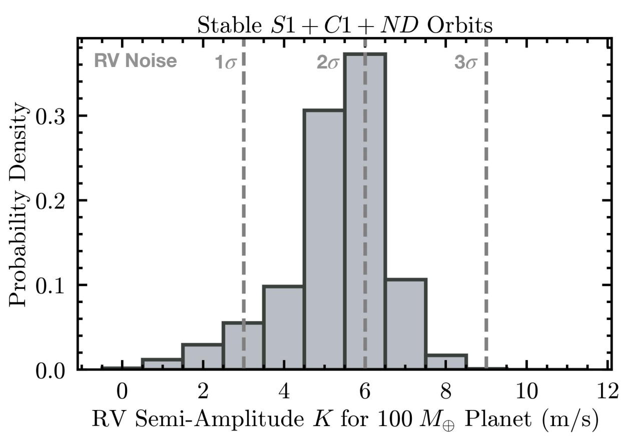

Figure 11. The RV semiamplitude of a 100 $M_\oplus$ planet in stable orbits fit to $S1 + C1$ and consistent with the nondetections in the 2025 February and April epochs. Note that K_{RV} scales linearly with planet mass. The systematic RV noise floor of 3 m s^{-1} (1σ; L. Zhao et al. 2018; P. Kervella et al. 2025, in preparation) is shown.

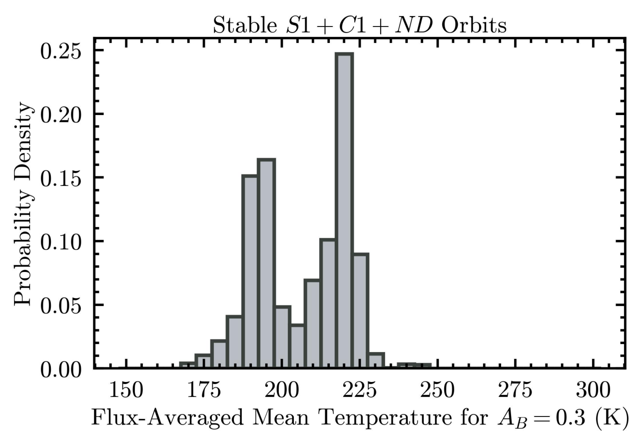

Figure 12. Range of flux-averaged mean planet temperatures for $A_B = 0.3$ corresponding to the orbits described in the preceding section. The lower temperatures in the bimodal distribution correspond to the $a > 2$ au orbits.

yields a model flux consistent with the measured photometry within 1σ. The effective temperature of the planet is set to 225 K for the atmospheric models fit below, matching that expected for $a < 2$ au orbits (Table 4).[28] We also restrict the surface gravity (log g, in cgs units) of the models to 2.5–3.0 dex, chosen to yield a planet mass $\lesssim$ 150–200 $M_\oplus$ to be consistent with the RV limits ($M_{\mathrm{p}} \sin i < 150$ $M_\oplus$, 3σ; inclined orbits can raise the limit on the true planet mass).

ATMO2020++. Using the ATMO2020 models. with strong vertical mixing as a starting point, ATMO2020++ (S. K. Leggett et al. 2021; A. M. Meisner et al. 2023) modifies the adiabatic ideal gas index γ (and thus atmospheric temperature gradient) to

[28] We were unable to fit the photometry with 200 K models for planet radii < 1.2 R_{Jup}.

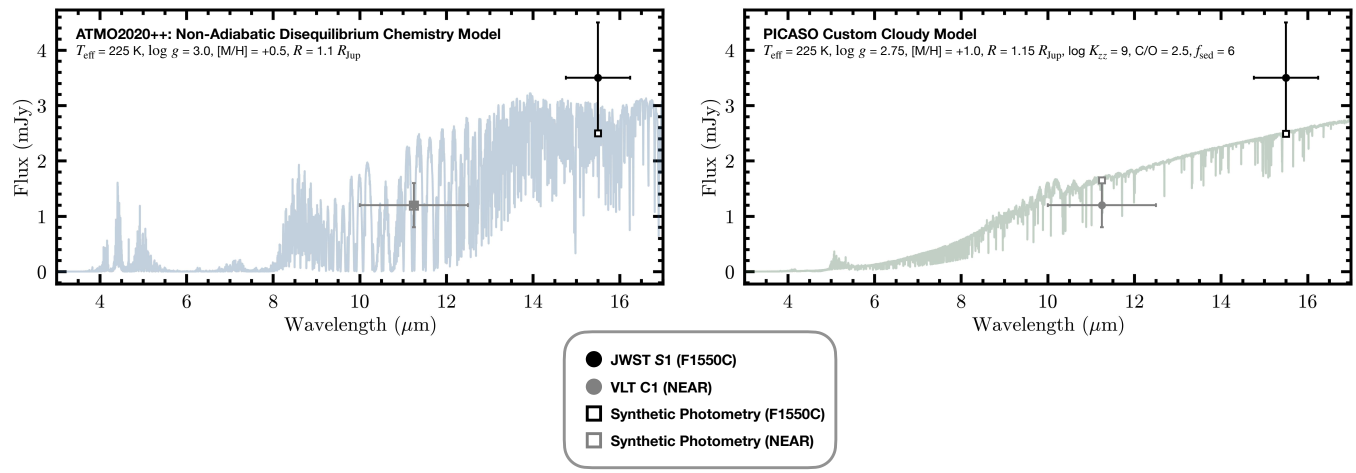

Figure 13. $T_{\rm eff} = 225$ K atmospheric models consistent with the $S1 + C1$ photometry (within 1σ) for a radius $< 1.2\ R_{\rm Jup}$.

account for the effect of processes responsible for producing a nonadiabatic cooling curve in giant planet and brown dwarf atmospheres. These processes include complex atmospheric dynamics (e.g., zones, spots, and waves) due to rapid rotation, compositional changes due to condensation, upper atmosphere heating by cloud decks or breaking gravity waves, etc. Recent modeling with JWST data have shown that this grid provides an improved fit to Y dwarf spectra compared to standard-adiabat models (S. K. Leggett & P. Tremblin 2023, 2024; K. L. Luhman et al. 2024). The default ATMO2020++ grid only extends to $T_{\rm eff} = 250$ K, so we generated custom models for $T_{\rm eff} = 225$ K, log $g = 3.0$ dex, and [M/H] $= +0.5$ and $+1.0$. We find that the $T_{\rm eff} = 225$ K, log $g = 3.0$ dex, and [M/H] $= +0.5$ model agrees with the photometry for a radius of 1.1 $R_{\rm Jup}$ (Figure 13). For the above parameters, the planet candidate would have a mass $\approx 150\ M_\oplus$.

Sonora and PICASO models. The Sonora Flame Skimmer models (J. Mang et al. 2025, in preparation) extend the cloud-free Sonora Elf Owl grid (S. Mukherjee et al. 2024; N. F. Wogan et al. 2025) to colder effective temperatures, lower surface gravities, and a broader range of metallicities. These models incorporate rainout chemistry for H_2O, CH_4, and NH_3—even in cloud-free atmospheres—similar to the treatment in Sonora Bobcat. They also address the underestimation of CO_2 found in the Sonora Elf Owl models (S. Mukherjee et al. 2024), which has since been revised in N. F. Wogan et al. (2025). In addition, we generated a custom grid of cloudy models using `PICASO` (N. E. Batalha et al. 2019; S. Mukherjee et al. 2023). This grid spans effective temperatures of $T_{\rm eff} = 200$ and 225 K, surface gravities of log $g = 2.75$ and 3.0 dex (cgs), eddy diffusion coefficients $K_{zz} = 10^2$ and 10^9 cm^2 s^{-1}, metallicities of [M/H] $= +0.5$ and $+1.0$, and a C/O ratio of 2.5 (relative to solar). Cloudy models have $f_{\rm sed} = [4, 6, 8]$, with H_2O as the only condensing species. We find that the $T_{\rm eff} = 225$ K, log $g = 2.75$ dex, [M/H] $= +1.0$, log $K_{zz} = 9$, C/O $= 2.5$, and $f_{\rm sed} = 6$ model agrees with the photometry for a radius of 1.15 $R_{\rm Jup}$ (Figure 13). For the above parameters, the planet would have a mass $\approx 90\ M_\oplus$.

Additional models applicable to cool giant planets. We also experimented with fitting the photometry using the Sonora Bobcat cloudless, chemical equilibrium model grid (M. S. Marley et al. 2021), the ATMO2020 solar metallicity, disequilibrium chemistry model grid (M. W. Phillips et al. 2020), the patchy water cloud models of C. V. Morley et al. (2014), and a new grid of self-consistent models by B. Lacy & A. Burrows (2023) that incorporate both the effects of water clouds and disequilibrium chemistry. However, we did not find suitable solutions with these grids, as they all required $T_{\rm eff} \geqslant 250$ K to fit the photometry for a radius $< 1.2\ R_{\rm Jup}$.

5.3. Planet Ring System Models

The previous section presented example planet models which can reproduce the brightness of $S1 + C1$, but required planet radii $\approx 1.1\ R_{\rm Jup}$ (driven by the observed F1550C brightness), more commonly observed for hotter planets, but plausible if a rapidly rotating planet is viewed closer to pole on (the observed surface area can be higher). Alternate explanations for the F1550C brightness include (1) a knot of exozodiacal emission or (2) a smaller planet with a circumplanetary ring. Given the lack of exozodi detection reported in Section 3.4, we do not consider the exozodi knot interpretation further, except to note that this would require the knot to dominate the exozodi emission, and for the knot to orbit the star with similar constraints to those reported for the planet scenario (Section 4) and to have only been detected at one epoch of our observations.

For an interpretation of the emission as circumplanetary material, a straightforward model is to consider an optically thick ring. A ring is not expected to have significant thermal inertia (as opposed to a gas giant planet, as discussed in Section 5.1). Thus, the ring temperature at the $S1$ and $C1$ detection epochs will be the instantaneous equilibrium temperature calculated for the true planet–star separation at those epochs. For each stable $S1 + C1$ orbit consistent with the nondetections in the prograde $a < 2$ au family, we calculate the planet–star separation and the corresponding equilibrium temperature, assuming $A_B = 0.1$ (similar to asteroids) and $f = 1$ (Figure 14). Orbits with $a < 2$ au are favored as they yield a higher planet $T_{\rm eq}$, which is required to better fit the F1550C brightness (the prograde and retrograde scenarios yield similar separation distributions and mean values). We find that an optically thick circumplanetary ring would be hotter at the $C1$ epoch ($T_{\rm eq} = 257 \pm 22$ K) than at the $S1$ epoch ($T_{\rm eq} = 209 \pm 11$ K).

We modeled the observed $S1 + C1$ photometry using various 225 K planet atmospheric models (grids discussed in Section 5.2) combined with a constant surface area (free parameter) BB ring with a temperature of 257 K for the VLT/NEAR 10–12.5 μm flux and a temperature of 209 K for the

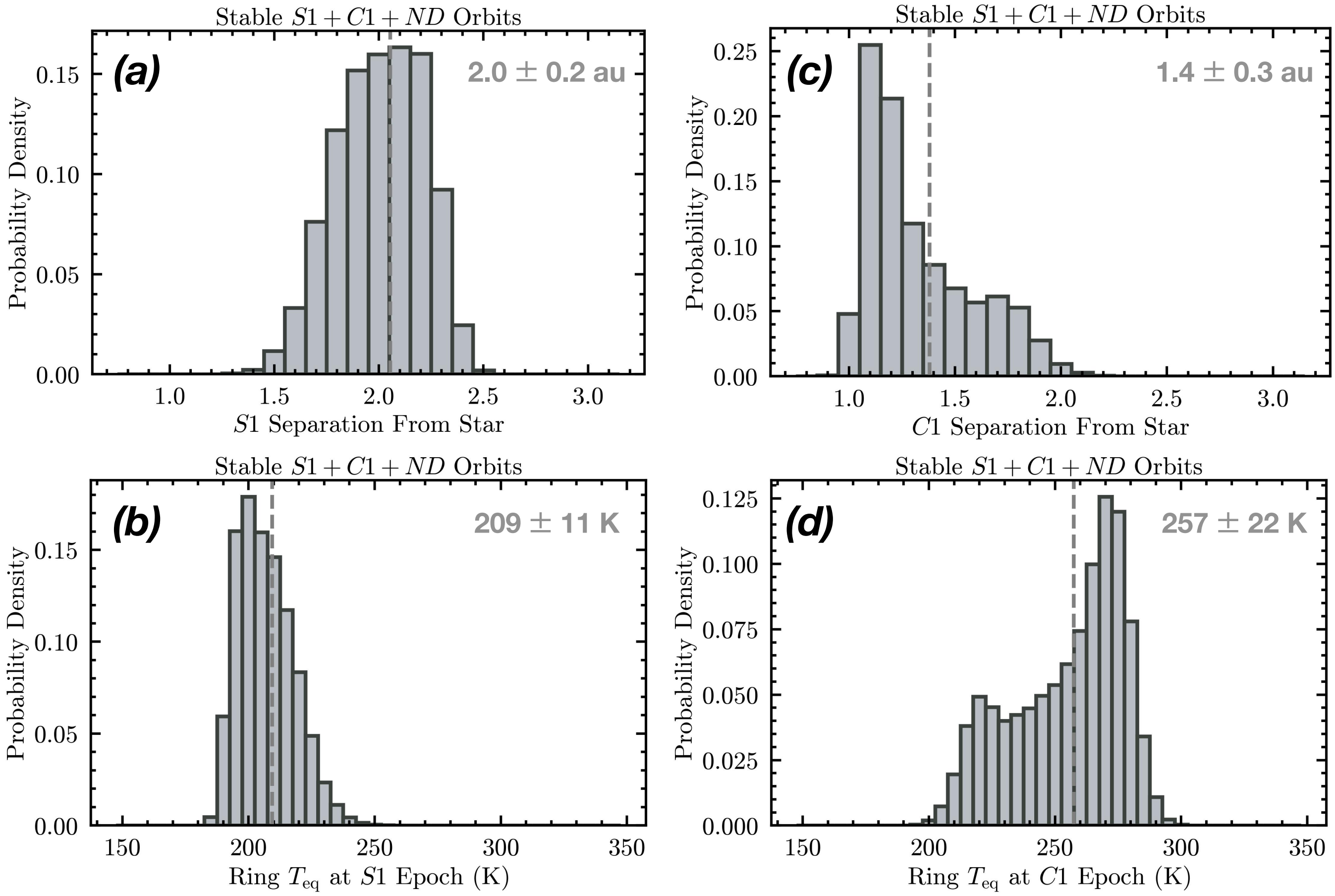

Figure 14. Range of (true) star–planet separations (top) and instantaneous temperatures (bottom) for a planetary ring with $A_B = 0.1$, no thermal inertia, and $f = 1$, seen at the epochs of $S1$ (left) and $C1$ (right) based on the stable orbits consistent with the nondetections in the prograde $a < 2$ au family as described in Section 4. The mean value of each distribution is marked with a dashed line and noted with the standard deviation in the top right corner of each panel.

F1550C flux. The photometry agrees, within the 1σ uncertainties, with a Sonora Flame Skimmer clear, equilibrium, $T_{\rm eff} = 225$ K, log $g = 3.0$ dex, [M/H] = +1.0, and C/O = 1.5 model for a planet radius of 1 $R_{\rm Jup}$ (corresponding to $\approx$120 $M_\oplus$), together with a ring that has a cross-sectional area equivalent to a face-on disk of radius $\approx$ 64,000 km or $\approx$0.9 $R_{\rm Jup}$ (Figure 15). This is $\sim$0.5 the cross-sectional area of Saturn's rings, which extend to 140,000 km (plus a more tenuous, more distant distribution). Planetary rings lie in their planet's Roche zone from 1.4 to 2.5 $R_{\rm p}$, so this explanation seems plausible. If the planet candidate is closer to the star at the $S1$ epoch or farther at the $C1$ epoch than the mean separation presently assumed at each epoch, then the agreement with the measured photometry improves.

We stress that the ring model discussed above is highly simplified. Geometrical effects make it challenging to develop a fully comprehensive and accurate optically thick ring model. The inclination of the ring with respect to the star affects the ring's temperature. The inclination of the ring to our line of sight together with shadowing of the ring by the planet affects the inferred size and visible emitting area. Additionally, a ring could both shade the planet from starlight, reducing the planet's temperature, and block planet light toward the observer. In the absence of strong constraints on the planet candidate's orbit and with only two photometric points, the problem is highly unconstrained. Overall, the key takeaway of the analysis presented above is that a circumplanetary ring around the $S1$ + $C1$ planet candidate is a plausible hypothesis

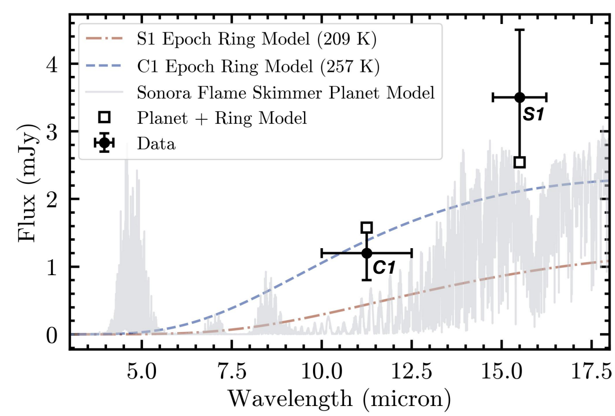

Figure 15. BB emission from a circumplanetary ring for a total cross-sectional area equivalent to the half the face-on cross-sectional area of Saturn's rings together with a fiducial planet atmospheric model ($T_{\rm eff}$ = 225 K, log $g = 3.0$ dex, [M/H] = +1.0, C/O = 1.5, and $R_{\rm p}$ = 1 $R_{\rm Jup}$). Each component contributing to the total model VLT/NEAR and F1550C flux (squares) is shown. There are two BB components as the ring temperature is different for each detection epoch, depending on the planet–star separation in Figure 14.

to explain the higher F1550C brightness for a smaller planet than inferred just using atmospheric models. A summary of the inferred mass and radius of the $S1$ + $C1$ candidate from both atmospheric and ring models, as compared with the cold transiting planet population, is presented in Figure 16.

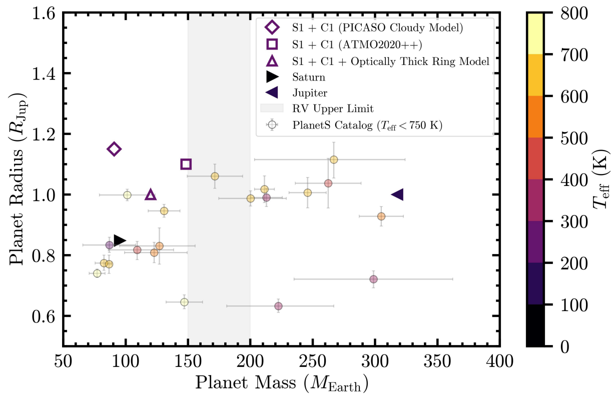

Figure 16. Observed masses and radii derived from transit observations for planets cooler than 750 K (from the Planets Catalog; S. Müller et al. 2024) are shown along with the properties of the $S1 + C1$ planet candidate inferred from the different models. The shaded area shows the approximate range of RV upper limits, depending on the exact inclination of the candidate's orbit. The positions of Saturn and Jupiter are included.

For completeness, we consider an alternative model for circumplanetary material, where the cross-sectional area derived above comes from an optically thin dust distribution, such as one that might arise from the grinding down of a cloud of irregular satellites orbiting the planet (G. M. Kennedy et al. 2011). Such a cloud could extend out to roughly half the Hill radius of the planet ($R_{\rm H} \sim 0.09$ au radius for a low eccentricity, $100\,M_\oplus$ planet at 2 au), which would correspond to a distribution with optical depth $\sim 5 \times 10^{-5}$. Small grains with realistic optical properties, in models in which the dust is optically thin, are heated above the BB temperature. This increases the flux in the VLT/NEAR bandpass and makes it more challenging to simultaneously fit the $S1$ and $C1$ photometry, specifically because the ring is expected to have a higher temperature at the $C1$ detection epoch than the $S1$ detection epoch from planet–star separation calculations (Figure 14). This would require the dust distribution to be truncated to avoid the presence of micron-sized dust. This is in addition to the challenge of retaining the irregular satellites given their expected collisional erosion.

6. Discussion

We start by investigating possible mechanisms to explain the high eccentricity and inclination orbits inferred for the $S1 + C1$ candidate in a close binary system like α Cen AB. We then briefly discuss the prospects for other planets or an exozodiacal disk around α Cen A in the presence of the $S1 + C1$ candidate, and end with a discussion of the implications of a gas giant in α Cen AB system in relation to theories of planet formation in binary systems.

6.1. Planetary Companions

6.1.1. Secular Dynamics of the S1 + C1 Planet Candidate

Table 4 reveals that the best-fitting orbits for $S1 + C1$ consistent with the nondetections are significantly inclined with respect to the α Cen AB binary orbital plane and eccentric, which naturally leads one to suspect that the planet candidate might undergo von Zeipel–Kozai–Lidov (vZKL) oscillations. The vZKL mechanism is a secular gravitational effect in hierarchical triple systems whereby a distant companion's torque drives a periodic exchange between the inner orbit's eccentricity and inclination. This dynamical exchange can help explain why the candidate planet's best-fitting orbits exhibit moderate eccentricity, as it cycles through a wide range of eccentricities and mutual inclinations (H. von Zeipel 1910; Y. Kozai 1962; M. L. Lidov 1962; T. Ito & K. Ohtsuka 2020). In the test particle approximation (S. Naoz 2016) for vZKL oscillations, the less massive body ($S1 + C1$) will have a minimum mutual inclination $i_{\rm mut}$ relative to the more massive binary, which is approximately 39°.2 for prograde and 141°.8 for retrograde orbits. Figure 17 shows the probability density of minimum inclination attained during our N-body stability simulations selecting on the stable orbits that fit $S1 + C1$ and are consistent with the nondetections. The minimum mutual inclination shows that a majority of orbits undergo vZKL oscillations, likely to be large amplitude, in the test particle approximation and are consistent with the candidate's present configuration.

6.1.2. Prospects For Other Planets Orbiting α Cen A

The Hill radius, $R_{\rm H}$, gives a measure of the relative gravitational influence of two bodies on a third and can be used to identify regions in the semimajor axis for the stability of a third body. We use this to assess the possibility that another planet might exist in the HZ of α Cen A given the presence of a planet with the properties of $S1 + C1$. The Hill radius, $R_{\rm H}$ is given by

$$R_{\rm H} \approx a(1 - e)\sqrt[3]{\frac{m_{\rm p}}{3(m_* + m_{\rm p})}}. \tag{4}$$

Given the best-fit semimajor axis, a, and eccentricity, e, for each of the potential orbital families (Table 4), using the host star mass ($m_\star = 1.08\,M_\odot$), and assuming a candidate planet mass ($m_{\rm p} \sim 100\,M_\oplus$), the Hill radius R_H for semimajor axis, $a = 1.62$–2.16 au and eccentricity ~ 0.4, ranges from 0.044 to 0.060 au. B. Quarles et al. (2018) argue that for stability in a coplanar system, a buffer zone of $\approx 7.5\ R_{\rm H}$ is required to establish stable orbits in a two planet system. Thus, it is unlikely for there to be any other planets between $a(1 - e) - 7.5\ R_{\rm H}$ and $a(1 + e) + 7.5\ R_{\rm H}$, i.e., from 0.6 to 3.5 au, depending on the value of a. Thus, assuming the $S1 + C1$ candidate is real, there are probably no other planets within or exterior to α Cen A's HZ.

These arguments are bolstered with numerical simulations which show, with the parameters of $S1 + C1$, there are no stable orbits exterior to ∼0.5 au (Figure 18). These simulations use the N-body simulation package `Rebound` with the `IAS15` integrator, where the massive bodies (binary + $S1 + C1$) begin with the mean orbital parameters from the $K_{\rm RV} < 3\ {\rm m\,s^{-1}}$ cases in Table 4 for $S1 + C1$ and stellar parameters from R. Akeson et al. (2021). The putative second planet begins as a test particle on a slightly eccentric orbit ($e_{\rm p}^* = 0.05$) that is apsidally aligned and coplanar with $S1 + C1$, where we vary the putative second planet semimajor axis $a_{\rm p}^*$ from 0.25 to 3 au with steps of 0.001 au and initialize the mean anomaly of the body from 0° to 359° in steps of 1°. The simulations are evolved for 1 Myr, where an individual simulation is stopped depending on the state of the test planet, which can either be ejected (distance $r_{\rm p}^*$ of the test planet exceeding 5 au), have high eccentricity ($e_{\rm p}^* > 0.95$), or collide with either $S1 + C1$ or the host star.

From these simulations, we calculate the lifetime t_{99} when 99% of the test particles are unstable (in Figure 18(a)) and the

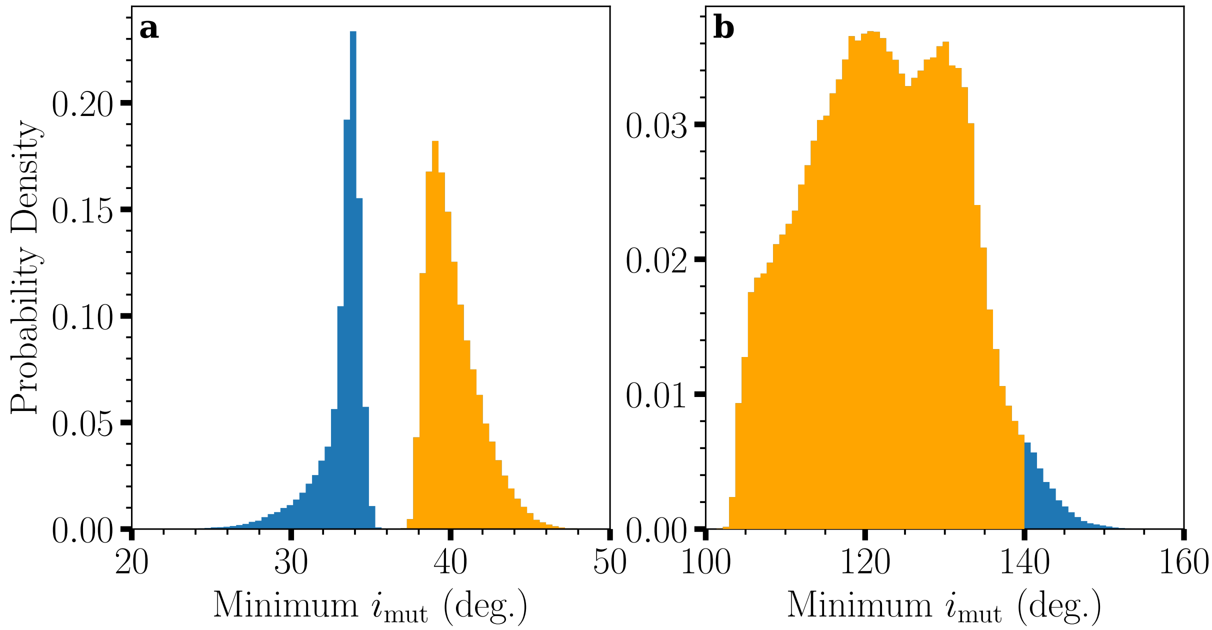

Figure 17. Range of minimum mutual inclination $i_{\rm mut}$ experienced by the prograde (a) and retrograde (b) planet in the inner orbit (a < 2 au family). Orbits colored yellow represent the $i_{\rm mut}$ range within the vZKL regime that would produce large amplitude oscillations, while blue denotes $i_{\rm mut}$ values that would have much lower oscillations.

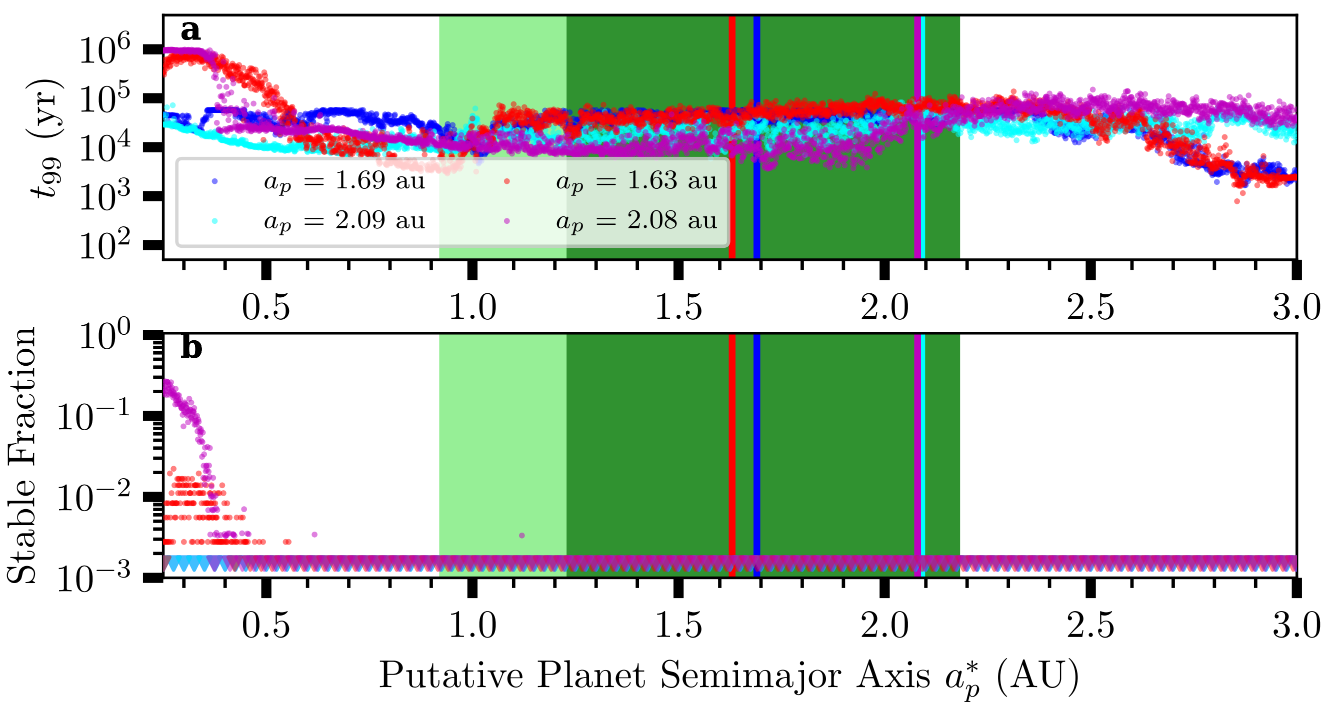

Figure 18. The planet candidate is initialized using the mean values from Table 4 with $K_{\rm RV}$ < 3 m s^{-1}, where the color-coded points denote the planet candidate with a prograde (blue/cyan) or retrograde (red/magenta) orbit. The top panel shows the lifetime t_{99} when 99% of the test particles are unstable, while the bottom panel measures the fraction of stable particles for a given initial semimajor axis. The triangles denote upper limits for the stable fraction due to the finite number of trials (360) per semimajor axis. The light green region denotes the optimistic HZ, while the dark green represents the more conservative HZ.

fraction of test particles that are stable for a given semimajor axis (in Figure 18(b)). For $a_{\rm p}^* \gtrsim 0.5$ au, virtually all test particles are unstable within 10^5 yr, while for $a_{\rm p}^* \gtrsim 0.4$ au very few remain in orbit for 1 Myr. The prospects for stability for the test particles increase for $a_{\rm p}^* \lesssim 0.4$ au, but only when considering a retrograde-orbiting planet candidate. In summary, Figure 18(b) strongly suggests that the region exterior to ∼0.4 au will be inhospitable to any other planets in the presence of $S1 + C1$. The dynamics of the α Cen AB system were already known to be inhospitable to planets outside of ∼3 au (B. Quarles & J. J. Lissauer 2018).

6.1.3. Planets in Binary Systems

Planets in multiple star systems are not rare. As of this writing, the NASA Exoplanet Archive (J. L. Christiansen et al. 2025) lists

Table 5
Known S-type Planetary Systems with Similar Orbital Architecture as α Cen AB + $S1$ + $C1$

Planetary System	$a_{\mathrm{A-B}}$ (au)	$e_{\mathrm{A-B}}$ (au)	$a_{\mathrm{A-Ab}}$ (deg)	$e_{\mathrm{A-Ab}}$	i_{mutual}	References
α Cen AB + $S1$ + $C1$ Candidate	≈23	≈0.5	≈1.6 or ≈2.1	≈0.4	≈50 or ≈130	(1, 2)
HD 196885 AB + HD 196885 Ab	≈21	≈0.4	≈2.6	≈0.5	≈25	(3)
γ Cep AB + γ Cep Ab	≈19	≈0.4	≈2.1	≈0.1	≈114	(4)

Note. The orbital parameters are generally well constrained in all cases but are quoted without uncertainties for the purposes of an approximate, order-of-magnitude comparison.

References. (1) R. Akeson et al. (2021); (2) This work; (3) G. Chauvin et al. (2023); and (4) X. Huang & J. Ji (2022).

over 500 such systems, although their number decreases with the number of stars (only 71 in triple systems such as α Cen AB + Proxima Centauri, i.e., α Cen ABC, but stellar companions that are as intrinsically faint as Proxima Centauri may not have been identified yet), including cases like Kepler-132 (KOI-284) where planets have been found in circumstellar orbits about both stars (J. J. Lissauer et al. 2014). There is strong observational evidence and robust physical arguments suggesting that for systems with $a < 100$ au, the formation of planets larger than sub-Neptunes in stable configurations is suppressed in multiple systems (A. L. Kraus et al. 2016; M. Moe & K. M. Kratter 2021; T. J. Dupuy et al. 2022; K. Sullivan et al. 2024). M. Moe & K. M. Kratter (2021, their Figure 3) describe a suppression factor of 0.4 for a binary system with α Cen AB's semimajor axis of 23 au. Yet although there is observational evidence for the suppression of planet formation in binary systems, there are numerous analyses of multiple star systems which show islands of stability close to either or both of the stars in multiple systems (B. Quarles & J. J. Lissauer 2016, 2018). Two systems in particular, HD 196885 AB + HD 196885 Ab and γ Cep AB + γ Cep Ab, are notable for their similarity in S-type orbital architectures to the candidate α Cen AB + $S1$ + $C1$ system (Table 5). In each case, the stellar system is a close, eccentric binary and hosts a moderately eccentric planet that is inclined with respect to the stellar binary orbital plane (prograde or retrograde). Thus, the existence of an exoplanet with the properties of $S1$ + $C1$ in the α Cen AB system is not impossible.

6.2. Exozodiacal Disks

6.2.1. Exozodiacal Disks in Binary Systems

While the formation of circumstellar sub-Neptunes and larger planets appears to be significantly suppressed in close binaries like α Cen AB, the fate of the smaller bodies that constitute terrestrial planets and debris disks is more nuanced. On the one hand, there has so far been no clear detection of circumstellar debris disks in binaries of separations < 100 au by means of infrared excess (D. E. Trilling et al. 2007; B. Yelverton et al. 2019). But recent observational findings suggest that the presence of circumstellar super-Earths in such binaries is relatively less suppressed than that of sub-Neptunes (K. Sullivan et al. 2024). This implies that the early stages of planet formation, that is, planetesimal formation and accretion, remain relatively effective.

It is thus reasonable to assume that debris disks can form and exist around these objects, with the caveat that they must lie within the stable region around either stellar component, stretching only a small fraction of their separation, e.g., $\sim$12% in the case of α Cen AB (P. Thebault et al. 2021; N. Cuello & M. Sucerquia 2024). For binaries with similar separations, this suggests that only ABAs within a few astronomical units of each star are dynamically viable as circumstellar debris disks. Any dust produced from them would be relatively warm ($\sim$100–300 K), exozodiacal dust, and would emit predominantly in the mid-infrared—where it is outshone by the star—potentially explaining the lack of photometric detections.

Finally, recent observational studies indicate that the orbits of planets orbiting one of the stars in binary (an S-type exoplanet) are roughly aligned with the binary orbit, particularly for separations below $\sim$100 au. Astrometric monitoring of Kepler planet hosts in binaries has shown that mutual inclinations are typically small, likely within 0°–30° (T. J. Dupuy et al. 2022; K. V. Lester et al. 2023). These findings suggest that long-lived debris disks might exist and might be aligned with binary orbital plane.

6.2.2. Can an Exozodi Disk and an S1 + C1-like Planet Coexist around α Cen A?

The prospects of finding a stable debris disk orbiting a star in a binary system must also be considered in the context of the presence of planets. Figure 18 shows effect of a planet on the possibility of stable orbits either for other planets or for particles in a disk. This shows that even if a planetesimal belt was able to form in this system it would not be able to survive in the face of dynamical perturbations from both α Cen B, which prevents orbits surviving beyond $\sim$2.8 au (B. Quarles & J. J. Lissauer 2016), and a planet like the $S1$ + $C1$ candidate, which causes an unstable region that extends to within $\sim$0.4 au of α Cen A. While a planetesimal belt could survive interior to the planet, the current JWST/MIRI observations are not sensitive to any possible exozodi so close to the star.

6.3. Future Opportunities with α Cen A

The most pressing task for further work is to capture a second sighting of $S1$ with JWST. Figure 19 identifies an excellent opportunity in 2026 August to recover $S1$ based on the family of stable $S1$ + $C1$ orbits consistent with the nondetections described in Section 4. Around this date, the separation exceeds $\sim 1''$ and the predicted location is clear of the 4QPM boundaries. There is an urgency to this given the rapid approach of α Cen A to the known background star denoted KS5 (P. Kervella et al. 2016). Between mid-2027 and mid-2028, the two will be within $3''$ of one another. We note here that if $S1$ is unrelated to $C1$, then the orbits are much less constrained and there is significant uncertainty in its position at any given observation date. Additionally, there are numerous opportunities to follow-up the detection of the candidate exoplanet for further characterization with upcoming and future facilities.

1. The clear photospheric model has higher flux between 4 and 5 μm (Figure 15) compared to the nonadiabatic and

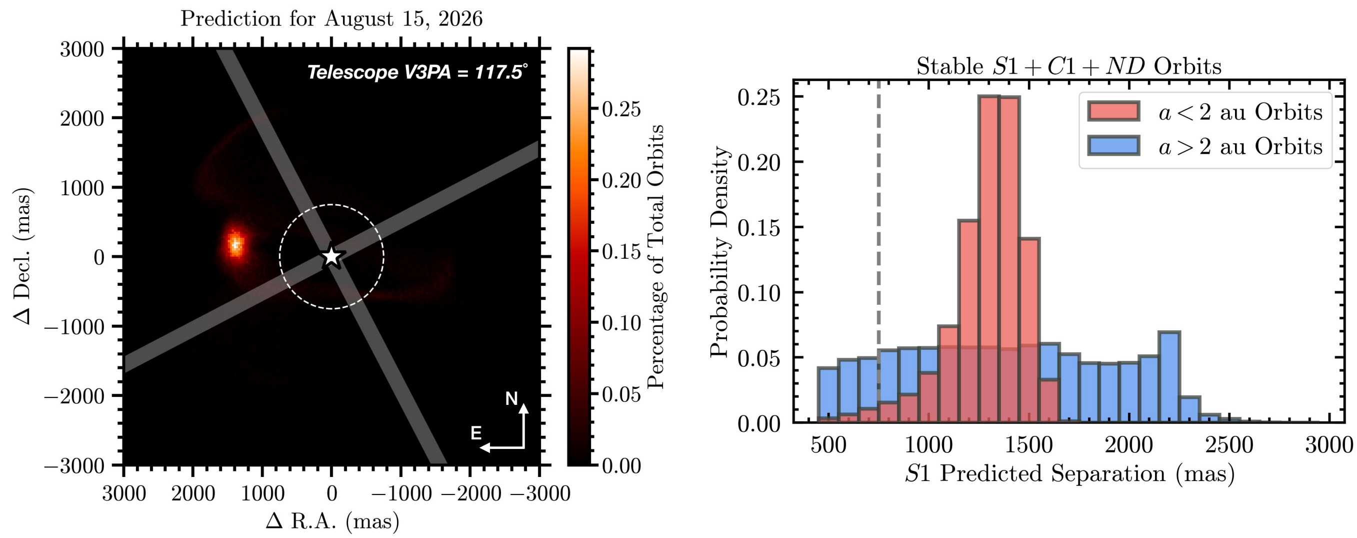

Figure 19. A prediction for the location of $S1$ based on the family of dynamically stable orbits for $S1 + C1$ consistent with the nondetections in 2025 suggests that $S1$ will be well positioned for recovery in 2026 August. Left: predicted position in sky coordinates. The approximate orientation of the 4QPM transition boundaries at the selected example observation date is shown as a shaded region. The dashed circle marks a 0.″75 separation. Right: histogram of the predicted separation of $S1$ in 2026 August for the two orbital semimajor axis families. A dashed line marks a 0.″75 separation. The $a < 2$ au orbits constitute a greater fraction of the total number of orbits and are also favored based on photometric modeling in Section 5.

cloudy models (Figure 13). NIRCam coronagraphy could serve as a powerful diagnostic tool for the different models presented.

2. The coronagraphic instrument on the Nancy Roman Space Telescope has a mask specifically designed to work in the presence of a binary star system (E. A. Bendek et al. 2021) and could be used to detect reflected visible light from a gas giant around 1–2 au.
3. The METIS instrument on the European Extremely Large Telescope should be capable of spectroscopic observations of the $S1$ candidate (J. Birkby & L. Parker 2024) and could even look for RV shifts in the motion of the planet due to the presence of an exomoon.
4. Direct mass measurements should be possible with additional RV monitoring and with differential astrometry at millimeter wavelengths with ALMA (R. Akeson et al. 2021), or at visible wavelengths with the proposed Toliman (P. Tuthill et al. 2018) or SHERA (J. Christiansen, private communication) space telescopes.
5. Finally, the proposed Habitable Worlds Observatory could, if equipped with appropriate binary star rejection capabilities, search for terrestrial-sized planets which might be found within the α Cen A system despite the pessimistic concerns about the stability of orbits exterior to 0.4 au (Section 6.1.2).

7. Conclusions

We conducted JWST/MIRI F1550C coronagraphic imaging observations of the nearest solar-type star, α Cen A, over three epochs between 2024 August and 2025 April to directly resolve α Cen A's HZ and perform a deep search for planets and exozodiacal disk emission. The key results from our program are summarized below.

Detection of a candidate gas giant exoplanet in orbit around our nearest Sun-like star, α Cen A. We detected a point source ($S1$) in the 2024 August epoch of JWST/MIRI 15.5 μm coronagraphic imaging. Detailed analysis, including various tests, presented in Paper II show that the source is unlikely to be a detector or speckle artifact. We definitively show that $S1$ is neither a foreground nor a background object. However, with only a single sighting by JWST, the candidate cannot be unambiguously confirmed as a bona fide planet.

Deep upper limits on an exozodiacal disk around α Cen A. These observations have set stringent upper bounds on the presence of extended "exozodiacal" dust disk in the HZ of α Cen A. A limit of $<$ 5–8$\times$ the dust level within our own zodiacal cloud (for a disk coplanar with the α Cen AB orbit) is a factor of $\gtrsim$10 more sensitive than those set by either photometric or interferometric methods toward more distant stars. Simulations show that for a planet with the candidate's properties, it is unlikely that a debris disk could remain stable and survive the planet's dynamical influence unless located within 0.4 au of the star.

Orbital properties of the α Cen A planet candidate. By linking the sighting of JWST/MIRI $S1$ to another candidate, $C1$, detected by the VLT/NEAR experiment in 2019, we found a set of dynamically stable orbits. 52% of the stable orbits were consistent with a nondetection of the planet candidate in the 2025 February and April epochs, indicating that it was likely missed in both follow-up observations due to orbital motion. The $S1 + C1$ candidate is in a highly inclined ($\approx$50° or $\approx$130° with respect to the α Cen AB binary orbital plane) and eccentric ($\sim$0.4) orbit, not unlike other S-type planets in close binary systems (e.g., HD 196885 Ab and γ Cep Ab), and is expected to undergo large amplitude vZKL oscillations.

Physical properties of the α Cen A planet candidate. $S1 + C1$'s effective temperature is set by heating from α Cen A and is expected to be $\sim$225 K based on the candidate's orbital properties. We found plausible atmospheric model solutions to the $S1 + C1$ photometry for a planet radius between $\approx$1.1–1.15 $R_{\rm Jup}$ and mass between 90–150 $M_\oplus$ (consistent with the RV limits). Alternatively, we showed that a simplified optically thick ring with a cross section equivalent to half of

Saturn's ring could increase the mid-infrared flux of a smaller ($\sim$1 R_{Jup}) planet to explain the estimated photometry.

Importance of a confirmed planet around α Cen A. A confirmation of the $S1$ candidate as a gas giant planet orbiting our closest solar-type star, α Cen A, would present an exciting new opportunity for exoplanet research. Such an object would be the nearest (1.33 pc), coldest ($\sim$225 K), oldest ($\sim$5 Gyr), shortest-period ($\sim$2–3 yr), and lowest-mass ($\lesssim$200 $M_{\oplus}$) planet imaged in orbit around a solar-type star, to date. Its extremely cold temperature would make it more analogous to our own gas giant planets and an important target for atmospheric characterization studies. Its very existence would challenge our understanding of the formation and subsequent dynamical evolution of planets in complex hierarchical systems. Future observations will confirm or reject its existence and then refine its mass and orbital properties, while multifilter photometric and, eventually, spectroscopic observations will probe its physical nature.

Acknowledgments

The STScI support staff provided invaluable assistance in the planning and execution of this program. In particular, we thank George Chapman and the FGS team for their dedicated work in finding and vetting guide stars for this program and Wilson Joy Skipper and the short- and long-range planning teams for their contributions to this challenging observational program. The STScI's Director's Office provided strong support for this program, from its initial selection as a high-risk, high-reward project, granting time to conduct test observations needed to validate the TA strategy, to the execution of the follow-up DDT programs. We gratefully acknowledge the ALMA Director's Discretionary Time program. In particular we wish to thank Richard Simon, Bill Dent, Brian Mason, Erica Keller, and Ilsang Yoon for their assistance in completing these critical observations in a timely manner. Dan Sirbu provided constructive comments on an earlier version of this manuscript. We thank the referee for a prompt report and helpful comments that improved this manuscript.

The specific observations analyzed can be accessed via doi: 10.17909/v8nv-vx17 for the 2024 August observations, doi: 10.17909/cb0x-rn85 for the 2025 February observations, and doi: 10.17909/3z9q-9f65 for the 2025 April observations. STScI is operated by the Association of Universities for Research in Astronomy, Inc., under NASA contract NAS5-26555. Support to MAST for these data is provided by the NASA Office of Space Science via grant NAG5-7584 and by other grants and contracts. This research has made use of NASA's Astrophysics Data System. Portions of this research were conducted with the advanced computing resources provided by Texas A&M High Performance Research Computing that was supported in part by the National Science Foundation (NSF) under grant #2232895. This Letter makes use of the following ALMA data: ADS/JAO. ALMA#2022.A.00017.S. ALMA is a partnership of ESO (representing its member states), NSF (USA) and NINS (Japan), together with NRC (Canada), MOST and ASIAA (Taiwan), and KASI (Republic of Korea), in cooperation with the Republic of Chile. The Joint ALMA Observatory is operated by ESO, AUI/NRAO, and NAOJ. The National Radio Astronomy Observatory is a facility of the National Science Foundation operated under cooperative agreement by Associated Universities, Inc. This work has made use of data from the European Space Agency (ESA) mission Gaia (https://www.cosmos.esa.int/gaia), processed by the Gaia Data Processing and Analysis Consortium (DPAC; https://www.cosmos.esa.int/web/gaia/dpac/consortium). Funding for the DPAC has been provided by national institutions, in particular the institutions participating in the Gaia Multilateral Agreement. This publication makes use of VOSA, developed under the Spanish Virtual Observatory (https://svo.cab.inta-csic.es) project funded by MCIN/AEI/10.13039/501100011033/ through grant PID2020-112949GB-I00. VOSA has been partially updated by using funding from the European Union's Horizon 2020 Research and Innovation Programme, under grant Agreement #776403 (EXOPLANETS-A). This research has made use of the NASA Exoplanet Archive, which is operated by the California Institute of Technology, under contract with the National Aeronautics and Space Administration under the Exoplanet Exploration Program.

This material is based on work supported by the National Science Foundation Graduate Research Fellowship under grant No. 2139433. Part of this work was carried out at the Jet Propulsion Laboratory, California Institute of Technology, under a contract with the National Aeronautics and Space Administration (80NM0018D0004). Program PID#1618, #6797, and #9252 are supported through contracts JWST-GO-01618.001, JWST-GO-06797.001, and JWST-GO-09252.001, respectively. Research done at NASA's Ames Research Center was supported by the NASA Astrophysics Division's Internal Scientist Funding Model (ISFM) program. This project is cofunded by the European Union (ERC, ESCAPE, project No 101044152). Views and opinions expressed are however those of the author(s) only and do not necessarily reflect those of the European Union or the European Research Council Executive Agency. Neither the European Union nor the granting authority can be held responsible for them.

Author Contributions

C.A.B. and A.S. led the writing and submission of this manuscript. C.A.B. developed the observational strategy and sequences in conjunction with D.H., J.A., and M.R. R.A. and E.F. executed and reduced the ALMA data. P.K. developed the detailed astrometric solution used for α Cen AB. A.S. led the postprocessing of the MIRI observations with the assistance of D.M., W.B., L.P., A.B., and J.L.-S. Analysis of the possible orbits of the α Cen A candidate was conducted by A.S., K.W., B.Q., and J.L. Photometric modeling of the α Cen A candidate was carried out by A.S. with the assistance of M.Z. and R.H. Custom atmospheric models were generated by J.M. and P.T. Dust emission models for the zodiacal cloud and an exoplanet ring system were developed by M.S., M.W., and C.A.B. Analysis of the extended emission was carried out by N.G. and E.C. All authors assisted with the preparation of the original JWST proposal and the manuscript.

Facilities: JWST (MIRI), ALMA, Gaia.

Software: `astropy` Astropy Collaboration et al. 2022), `emcee` (D. Foreman-Mackey et al. 2013), `jwst` (H. Bushouse et al. 2022), `multinest` F. Feroz et al. 2009), `NIRCoS` (J. Kammerer et al. 2022), `pyNRC` (J. Leisenring 2025, in preparation), `pysynphot` (STScI Development Team 2013), `spaceKLIP` (J. Kammerer et al. 2022), `matplotlib` (J. D. Hunter 2007), `numpy` (C. R. Harris et al. 2020), `scipy` (P. Virtanen et al. 2020), `STPSF` (M. D. Perrin et al. 2014), `webbpsf_ext` (J. Leisenring 2025, in preparation).

Appendix A
Details of the Observation Strategy

A.1. Reference Star Selection

For stars as bright as α Cen A (F1550C = −1.51 mag), the selection of reference stars is limited. The IRAS Low Resolution Spectrometer (LRS) Catalog (F. M. Olnon et al. 1986) was used to identify potential reference stars: $F_\nu(12\ \mu\mathrm{m}) > 50$ Jy within 20° of α Cen A, clean Rayleigh–Jeans photospheric emission, constant ratio (<10%) of LRS brightness ($F_{\alpha\ \mathrm{Cen\ A}}/F_{\mathrm{star}}$) across the F1550C band, a low probability of variability during the 300 day IRAS mission (VAR < 15%), and no bright companions within 100″. These criteria resulted in the selection of ϵ Mus (F1550C = −1.3 mag), a long-period variable star located 17° away on the sky with a K-band variability $\lesssim$ 0.5 mag (H. Murakami et al. 2007; V. Tabur et al. 2009). The ratio of the LRS spectra of the (unresolved) α Cen AB system to these stars is constant across the F1550C bandpass to <1%, which means that the effects of wavelength mismatches in the reference star subtraction will be negligible.

A.2. Target Acquisition

A.2.1. Astrometry of α Cen and ϵ Mus

The α Cen AB system has a parallax of 750 mas and an annual proper motion of (−3640, +700) mas yr^{-1}, which corresponds to a mean motion of ∼10 mas day^{-1}. The description of the procedures leading to the detailed ephemeris used for the observations are provided in R. Akeson et al. (2021). As described in Appendix B, the ephemeris is based on a combination of absolute astrometry from Hipparcos and ALMA. RV observations of both α Cen A and α Cen B help determine the motions of α Cen AB in their 80 yr orbit. The ephemeris was calculated on an hour-by-hour basis, including the effects of parallax as observed from the vantage point of JWST's L2 orbit (Figure A1). The location of JWST at L2, an additional 1.5 million km from Earth, increases the parallactic effect by 1% or 7.5 mas, but in a nonintuitive manner due to JWST's motion at L2 (Figure A2). This effect is not negligible compared to the θ_{LD} = 8.5 mas angular diameter of α Cen A (P. Kervella et al. 2017) and the centering accuracy requirement (∼10 mas) for best performance behind the MIRI coronagraphic mask (A. Boccaletti et al. 2022).

The precise location of JWST at the epoch of these observations was obtained from the JPL Horizons website.[29] The combination of visible data and two epochs of ALMA data (2018–2019; R. Akeson et al. 2021) and the 2023 ALMA DDT observations (described in Appendix B.1) for α Cen AB yields a precision of ∼2 mas in the predicted position of α Cen A (Figure A2 and Table A1). Taking into account the astrometric precision of the Gaia stars and of α Cen itself, we estimate that the overall astrometric precision of the blind offset between the offset stars and the two targets, ϵ Mus and α Cen A, will be ∼2.5 mas (1σ), to which must be added the ∼5–7 mas (1σ, one axis) offsetting precision of JWST itself.[30] Astrometry for ϵ Mus, its associated Gaia offset star, and α Cen A's associated Gaia offset star was obtained from the Gaia DR3 catalog (Table A2). The effects of the proper motion

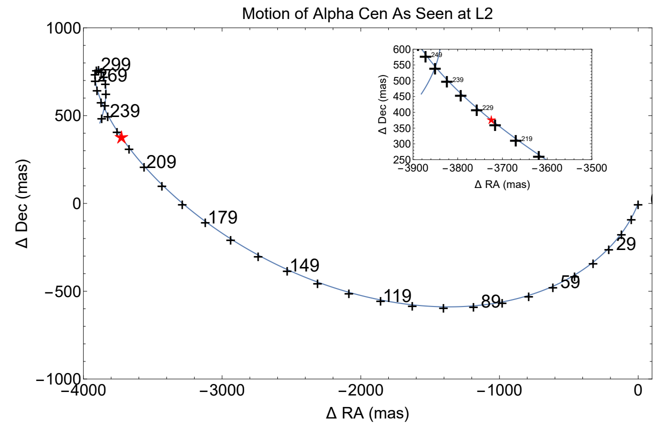

Figure A1. The change in the position of α Cen A relative to 2024 January 1 ($\Delta\alpha = 0$, $\Delta\delta = 0$) computed using proper motion and parallax as seen from JWST's L2 vantage point. Markers denote 10 day intervals and days of the year. As a reference, the red star denotes the date of the 2024 August JWST observations (first epoch). The inset plot zooms in near the 2024 August observation date with markers spaced in 5 day intervals. Details of the astrometry for α Cen are given in Appendix B and in R. Akeson et al. (2021).

and parallax values were taken into account but were relatively minor compared to those for α Cen A.

In planning the observational sequences in the Astronomer's Proposal Tool (APT), we specified the exact V3 rotation angles (with a precision of 0°.001) for each observation and used that information to derive the shift from the Gaia offset star to either α Cen A or ϵ Mus in instrument (x, y) coordinates. For α Cen A, these calculations used the position of α Cen A (including proper motion, parallax, and other smaller effects; R. Akeson et al. 2021) at the expected midpoint of the observation based on a detailed timeline of each observation (Table A3). The small amount of smearing during the 2.8 hr duration of each α Cen A observation (<2 mas) was deemed acceptable compared to the complexity of designating α Cen A as a moving target. The conversion of the offset in ($\Delta\alpha$, $\Delta\delta$) to instrument (x, y) was calculated for the exact epoch of observation and desired V3 angle using a model of the MIRI focal plane using STScI's pysiaf routine.[31]

A.2.2. Offset Star Selection and Validation

The offset stars used for TA were drawn from the Gaia DR3 catalog and had to have a mid-infrared brightness suitable for easy measurement in a short TA observation. A preliminary search of DR3 revealed 92 targets within 60″ of α Cen A and 24 within 30″ of ϵ Mus. Cuts in magnitude (G < 16 mag) and the requirement that each star have a quoted parallax and proper motion measurement reduced the number to a handful for each source. However, the proximity of both α Cen and ϵ Mus to the Galactic plane (b = −0°.67 and −5°.30, respectively) means that the effects of extinction can make predictions of mid-infrared brightness highly uncertain. For this reason, we scheduled test observations of both α Cen and ϵ Mus in the MIRI TA filter (F1000W) without any associated coronagraphic observations. These were executed in 2023 June. Figure 1 shows images of α Cen and ϵ Mus. Simulations using STPSF were developed to assess the influence of the bright target stars (α Cen A, α Cen B, and ϵ Mus) to ensure that diffraction effects would not affect the detectability of the much fainter Gaia stars in the TA procedure.

[29] https://ssd.jpl.nasa.gov/horizons/app.html#/

[30] https://jwst-docs.stsci.edu/jwst-observatory-characteristics-and-performance/jwst-pointing-performance#gsc.tab=0

[31] https://github.com/spacetelescope/pysiaf

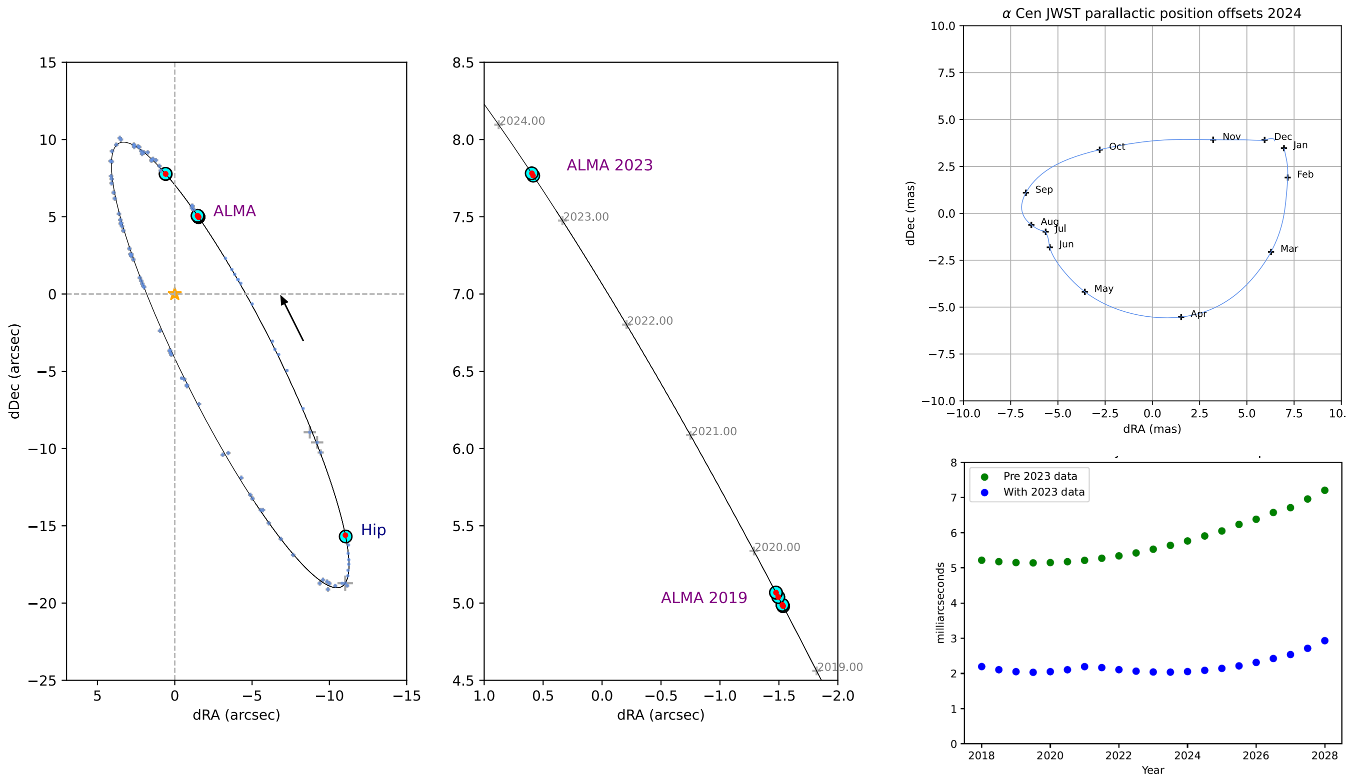

Figure A2. Left: orbit of α Cen B relative to α Cen A showing one epoch of Hipparcos and two epochs of ALMA data. Center: zoom-in view showing the ALMA data. Top right: the difference between the parallax effect as seen from Earth and from JWST at L2. Bottom right: the uncertainty in position of α Cen as a function of year before and after the addition of the new 2023 ALMA observations.

Table A1
Position of α Cen A at JWST Observation Epochs

Date (DD/MM/YYYY)	JD	R.A. (deg)	R.A.[a] (s)	Decl. (deg)	Decl.[b] (arcsec)
08/10/2024	2460750.363	219.84748601	(23.3967)	−60.83161739	(53.8226)
02/20/2025	2460727.234	219.8472157	(23.3318)	−60.8317325	(54.2370)
04/25/2025	2460790.995	219.8464966	(23.1592)	−60.83177278	(54.3820)
04/25/2025	2460791.2344	219.8464935	(23.1584)	−60.8317725	(54.3813)

Notes.
[a] Relative to $\alpha = 14^{h}39^{m}$.
[b] Relative to $\delta = -60°49'$. Positions incorporate proper motion and parallax as seen from the vantage point of JWST.

The star denoted $G0$ was suitable for both of the V3 roll angles selected for 2024 August and 2025 February (Table A2). The star denoted $G5$ was used for 2025 April. A single star ($G9$) was suitable for use with ϵ Mus at its V3 angle of observation in all three epochs.

A.3. Minimizing the Effects of Telescope Slews

The ability to detect faint companions is dominated by the stability of the wavefront of the JWST telescope and the accurate placement of the star behind the coronagraphic mask. Prelaunch expectations were that there would be slow-varying WFE drifts ∼10 nm depending on changes in solar elongation (and thus in the telescope's thermal balance) and due to stresses from internal structures such as the "frill" surrounding the primary mirror (M. D. Perrin et al. 2018). The on-orbit performance proved to be significantly better than prelaunch estimates, particularly as the telescope assembly continued to stabilize thermally, with drifts as low as ∼2–5 nm as measured using semidaily WFE monitoring observations (C.-P. Lajoie et al. 2023; J. Rigby et al. 2023). One factor in selecting the requested observing window was minimizing the change in solar elongation angle between α Cen and ϵ Mus. The final scheduled dates in 2024 August, 2025 February, and 2025 April resulted in changes in the absolute value of the solar angle of $\lesssim 10°$ (Figure A3). To mitigate further the effects of wavefront drift, we bracketed observations of α Cen with observations of ϵ Mus. This choice provided redundancy against any failure during guide star acquisition and TA by the telescope and thus would still leave one valid PSF reference star observation. Indeed, this proved to be important for the 2024 August observations where one ϵ Mus reference observation failed.

A.4. Mitigating the Effects of α Cen B

We initially considered strategies either using α Cen B as a reference star for α Cen A or placing α Cen B along the

Table A2
Gaia Astrometry for ϵ Mus and Offset Stars

Star	Gaia ID	R.A. (2016.0) (deg)	Decl. (2016.0) (deg)	$\mu_{\mathrm{R.A.}}$ (mas yr^{-1})	$\mu_{\mathrm{Decl.}}$ (mas yr^{-1})	Parallax (mas)	Total Uncertainty[a] (mas)	F_ν (F1000W)[b] (μJy)
ϵ Mus	5859405805013401984	184.3887799	−67.960909	−230.60 ± 0.19	−26.21 ± 0.26	9.99 ± 0.20	2.68	⋯
ϵ Mus TA[c] ($G9$)	5859405804986931200	184.3941452	−67.953630	−7.11 ± 0.02	0.43 ± 0.02	0.14 ± 0.02	0.21	13450
α Cen TA[d] ($G0$)	5877725249280411392	219.8776270	−60.828383	−1.79 ± 0.11	−1.01 ± 0.11	0.32 ± 0.09	1.28	1350
α Cen TA[e] ($G5$)	5877725146201190144	219.8800796	−60.8445635	−2.71 ± 0.17	−2.63 ± 0.28	0.001 ± 0.230	0.23	580

Notes.
[a] Combined uncertainty from parallax and proper motion between 2016.0 and 2024.3.
[b] Flux density measured in the 2023 June test images.
[c] Offset star used for TA of ϵ Mus in all three epochs.
[d] Offset star used for TA of α Cen A in 2024 August and 2025 February.
[e] Offset star used for TA of α Cen A in 2025 April.

Table A3
Log of Successful JWST/MIRI Observations of α Cen A

PID Obs. #	Target	No. Dithers	Science Time (hr)	Start Date and Time (DD/MM/YYYY UTC)	Observation Midpoint (UTC)	MIRI (x, y) Offsets[a] (arcsec)
1618-11	α Cen Snapshot (F1000W)[b]	4	0.19	06/19/2023 10:00	⋯	⋯
1618-50	ϵ Mus Snapshot (F1000W)[b]	4	0.19	06/19/2023 10:00	⋯	⋯
1618-61	ϵ Mus Snapshot (F1550C)	1	0.04	07/07/2024 22:31	⋯	⋯
1618-62	α Cen Snapshot (F1550C)	1	0.04	07/08/2024 00:29	⋯	⋯
1618-63	ϵ Mus Background (F1550C)	1	0.04	07/08/2024 02:21	⋯	⋯
1618-64	α Cen Background (F1550C)	1	0.04	07/08/2024 02:52	⋯	⋯
1618-52	ϵ Mus Visit 1 (V3 = 135.°0)	9	7.19	08/11/2024 13:00	08/11/2024 17:04	(−47.7588, −5.2736)
1618-53	ϵ Mus Visit 1 Background	1	0.80	08/11/2024 21:16	⋯	⋯
1618-56	Alpha Cen Roll 2 (V3 = 112.°7)	1	2.50	08/12/2024 04:56	8/12/2024 06:32	(32.7863, 42.8539)
1618-57	Alpha Cen Visit 2 Background	1	2.50	08/12/2024 08:09	⋯	⋯
1618-65	ϵ Mus at α Cen B (V3 = 135°)	1	0.80	08/12/2024 17:11	08/12/2024 18:48	(−39.372, −8.104)
6797-01	ϵ Mus Visit 1 (V3=133.°0)	9	7.19	02/20/2025 01:00	02/20/2025 04:57	(46.9405, −9.7562)
6797-02	ϵ Mus Visit 1 Background	1	0.80	02/20/2025 09:04	⋯	⋯
6797-03	ϵ Mus at α Cen B	1	0.80	02/20/2025 10:13	02/20/2025 11:42	(38.4623, −7.294)
6797-06	α Cen Roll 2 (V3 = 294.°5)	1	2.50	02/20/2025 19:51	02/20/2025 21:20	(−38.7111, −38.6047)
6797-07	α Cen Roll 2 Background	1	2.50	02/20/2025 23:10	⋯	⋯
6797-08	ϵ Mus Visit 2 (V3 = 133.°0)	9	7.19	02/21/2025 02:17	02/21/2025 06:15	(46.9399, −9.7563)
6797-09	ϵ Mus Visit 2 Background	1	0.80	02/21/2025 10:22	⋯	⋯
6797-10	ϵ Mus at α Cen B (V3 = 133.°0)	1	2.50	02/21/2025 11:30	02/21/2025 13:00	(38.629, 6.781)
9252-01	ϵ Mus Visit 1 (V3 = 38.°0)	9	7.19	04/25/2025 01:00	04/25/2025 04:57	(10.96213, −46.62994)
9252-02	ϵ Mus Visit 1 Background	1	0.80	04/25/2025 09:04	⋯	⋯
9252-03	ϵ Mus at α Cen B	1	0.80	04/25/2025 10:13	04/25/2025 11:42	(8.01166, −38.20160)
9252-04	α Cen Roll 1 (V3 = 346°)	1	2.50	04/25/2025 13:35	04/25/2025 15:04	(−50.83941, −54.82857)
9252-05	α Cen Roll 1 Background	1	2.50	04/25/2025 16:53	⋯	⋯
9252-06	α Cen Roll 2 (V3 = 356°)	1	2.50	04/25/2025 19:51	04/25/2025 21:20	(−59.593412, −45.16806)
9252-07	α Cen Roll 2 Background	1	2.50	04/25/2025 23:10	⋯	⋯
9252-08	ϵ Mus Visit 2 (V3 = 38.°0)	9	7.19	04/26/2025 02:17	04/26/2025 06:15	(10.96213, −46.62994)
9252-09	ϵ Mus Visit 2 Background	1	0.80	04/26/2025 10:22	⋯	⋯
9252-10	ϵ Mus at α Cen B (V3 = 38.°0)	1	2.50	04/26/2025 11:30	04/26/2025 13:00	(9.51997, −37.81736)

Notes. All F1550C coronagraphic data were obtained with FASTR1 using 30 groups with 400 integrations for ϵ Mus (behind 4QPM) and 1250 integrations for α Cen A (behind 4QPM) and ϵ Mus at the off-axis position of α Cen B. Observations 1618-1 to 1618-8 were obtained on 2023 July 26 and 2023 July 27, respectively, but failed due to either guide star issues or incorrect offsets from the Gaia stars. Observations 1618-54 and 1618-58 in 2024 August and 6797-04 in 2025 February failed due to guide star issues.
[a] Offsets from the Gaia star to the target star were calculated based on the epoch positions using the STScI software `pysiaf`.
[b] The F1000W broadband image was obtained with FASTR1 using 60 groups.

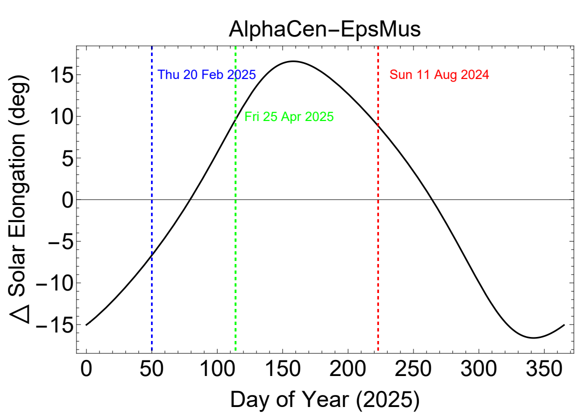

Figure A3. Change in the solar elongation angle between α Cen and ϵ Mus as a function of the day of year. The red, blue, and green dashed vertical lines correspond to the observation dates in 2024 August, 2025 February, and 2025 April, respectively.

quadrant boundaries of 4QPM to suppress its starlight. Both strategies had significant disadvantages. In the former case, the brighter star α Cen A would be unocculted on the detector in the reference images. In the latter case, very few opportunities were available to schedule observations in the desired configuration. Furthermore, small errors in the position of α Cen B along the boundaries would lead to substantial stellar leakage and changes in the PSF. Our prelaunch simulations and current data analysis demonstrated that the influence of α Cen B at 7″–9″ separation is sufficiently large in the 1″–2″ region around α Cen A that it is necessary to subtract the image obtained by placing ϵ Mus, unocculted but through the F1550C mask, at the same offset of α Cen B relative to α Cen A to provide an off-axis PSF reference. Analysis with the test observations obtained in 2024 July showed that the use of `STPSF` models was inadequate to remove speckles from α Cen B at the required level.

A.5. Mitigation of MIRI's Background: The "Glow Stick"

Following practice recommended by STScI to mitigate the effects of the Glow Stick phenomenon (excess telescope background scattered off of the telescope's structure; A. Boccaletti et al. 2022; A. L. Carter et al. 2023), we included MIRI background observations in exactly the same detector and instrument setup as the on-target observations for both ϵ Mus and α Cen. These background observations were placed in positions which appeared relatively blank in Spitzer or Wide-field Infrared Survey Explorer images. Each background field was observed twice for each object (Table A3) with 5″ shifts in the center position to help mitigate the effects of sources in the fields.

Appendix B
Astrometry of the α Cen System

Determining the astrometric properties of the α Cen system is complex due to the proximity of α Cen to Earth and the orbits of the two stars around their common center of mass. High-precision visible light observations are scarce due to the brightness of the two stars relative to much fainter reference stars. R. Akeson et al. (2021) made millimeter-wavelength observations of α Cen AB using the ALMA array. At these wavelengths, the two stars are bright enough to yield high-S/N data with milliarcsecond precision in ∼1 hour of observing time with absolute positions on the International Celestial Reference System (ICRS) reference frame. The ALMA observations are described in Appendix B.1 and the astrometric information used for the JWST observations in Appendix B.2.

B.1. New ALMA Astrometry of α Cen AB

The positions of α Cen A and α Cen B were observed with ALMA between 2018 October 14 and 2019 August 26 using about 40 25 m antennas as described in detail in R. Akeson et al. (2021) and summarized here. The average observing frequency was 343.5 GHz, but the ALMA configurations varied and produced a resolution of 140, 33, 28, 62, and 62 mas for the five observing blocks. Each block was about 80 minutes long and consisted of about 120 scans, of which 15% included calibration sources. The pointing center of each experiment was located near the expected barycenter of the A and B stars to minimize errors caused by small antenna pointing offsets. The α Cen AB positions were determined using the phase referencing technique with the nearby quasar J1452-6502, with an ICRS position accuracy < 0.5 mas. This uncertainty produced the main limit to the absolute radio position of the AB system. However, the separation of the A and B stars do not depend on the quasar's positional accuracy and some of the atmospheric position jitter between the A and B stars also canceled. Further details of the reduction, imaging, and multicalibrator checks to the astrometric accuracy are given in R. Akeson et al. (2021).

New observations were obtained through an accepted ALMA DDT proposal on 2023 June 1, 17, and 26 (DDT proposal 2022.A.00017.S). The data were taken in Band 7 (343.5 GHz) with the correlator configured for maximum broadband sensitivity. The 2023 positions are listed in Table B1 and were derived from pipeline-processed data using additional analysis to determine the internal position uncertainties. Due to the large proper motion of α Cen, roughly 10 mas day^{-1} on average, the phase center tracking has a significant impact on the measured positions. For the 2023 June 1 observations, the α Cen A position was tracked with time, while for the 2023 June 17 and 26 observations, the phase center was located near α Cen A, but was not tracked with time.

The main improvement from the previous ALMA observations (R. Akeson et al. 2021) is the measurement of internal position errors. These were estimated by splitting each 50 minute experiment into three independent parts and then determining the mean stellar position and the error from the scatter among the three parts. The slight stellar motion during an hour observation (0.4 mas) is much less than that caused by the typical temporal "atmospheric" variations. For the 2023 June 17 and 26 observations, where the phase center was located near α Cen A, but was not tracked with time, the α Cen A and α Cen B 1σ position errors are about 1.5 mas. For the 2023 June 1 observation, during which the α Cen A position was phased tracked, the location of the absolute frame of the images is uncertain, resulting in a larger absolute position error estimate (Table B1).

The absolute star positions in the DDT observations are tied to the phase calibrator (J1408-5712) whose absolute position is measured by global very long baseline interferometric observations. Its absolute position has an uncertainty of about 1.5 mas, which is, unfortunately, relatively large for an ICRS source since it has not been observed very often. The calibrator is located only $5\overset{\circ}{.}4$ away from α Cen and is the closest of the brighter available calibrators. If the J1408-5712 position error and the α Cen A internal position errors are combined, then the ICRS absolute position errors should be no larger than 2 mas in R.A. and in Decl.

The separation between α Cen A and α Cen B was also obtained for these observations, again by splitting up each 50 minute experiment into three parts. The estimated separation error is less than 1 mas for the 2023 June 17 and 26 observations because much of the error that affect the absolute positions of A and B cancels when calculating the stellar position difference. The accuracy is mostly S/N limited. Since the A–B separation for the 2023 June 1 observation does not depend on the somewhat uncertain definition of the absolute coordinate grid, its accuracy is only a bit larger than the two later observations.

B.2. Astrometry of α Cen A, α Cen B, and α Cen AB

The analysis method for determining the astrometric properties of the α Cen AB system using the combined visible and ALMA data is described in R. Akeson et al. (2021). The updated orbit is visualized in Figure A2. Accurate knowledge of the position of α Cen A depends on accounting for the location of JWST at L2. The differences in the parallactic motion between the two observing sites, Earth and L2, is ∼±5 mas (Figure A2). Finally, we note that the addition of the ALMA DDT observations reduced the uncertainty in the positions of α Cen A from ∼5–6 mas to ∼2 mas through 2028 (Figure A2). A detailed analysis of the orbit of α Cen AB, including all ALMA epochs and new HARPS RV data will be presented in a forthcoming paper (P. Kervella et al. 2025, in preparation).

Table B2 lists the positions of α Cen A and α Cen B as seen from JWST's location (which is obtained from the HORIZONS database),[32] and lists the relative positions of α Cen A and α Cen B, which were used in positioning the reference star ϵ Mus at the position of α Cen B to mitigate the speckles from the unocculted star. The first few entries of the full ephemeris are displayed and the complete table is available in electronic form at doi: 10.5281/zenodo.16280658.

[32] https://ssd.jpl.nasa.gov/horizons/app.html#/

Table B1
New ALMA Astrometry

Date	Start Time (UT)	Star	R.A. (deg)	Decl. (deg)
2023 Jun 1	02:35	A	219°864944115 (±3 mas)	−60°848591790 (±3 mas)
		B	219°865261605 (±4 mas)	−60°846446520 (±4 mas)
		A−B	−0″5935 ± 0″0004	−7″6756 ± 0″0005
2023 Jun 17	01:55	A	219°850279410 (±1 mas)	−60°831926083 (±1 mas)
		B	219°850610280 (±1 mas)	−60°829773243 (±1 mas)
		A−B	−0″5806 ± 0″0005	−7″7502 ± 0″0005
2023 Jun 26	00:59	A	219°850180635 (±0.8 mas)	−60°831902697 (±1.1 mas)
		B	219°850518885 (±1.2 mas)	−60°829745590 (±1.2 mas)
		A−B	−0″5715 ± 0″0020	−7″7234 ± 0″0020

Table B2
Astrometry of α Cen A and α Cen B (2024–2027)

Julian Year	Date and Time	R.A. (α Cen A) (J2000, deg)	Decl. (α Cen A) (J2000, deg)	R.A. (α Cen B) (J2000, deg)	Decl. (α Cen B) (J2000, deg)	ρ(A→B) (arcsec)	θ(A→B) (deg, north = 0)
2024.0000000	2024-01-01T12:00:00.000	219.84969992	−60.83174299	219.85019709	−60.82949888	8.1258	6.1630
2024.0027379	2024-01-02T12:00:00.000	219.84969758	−60.83174528	219.85019558	−60.82950072	8.1275	6.1721
2024.0054757	2024-01-03T12:00:00.000	219.84969512	−60.83174758	219.85019396	−60.82950258	8.1293	6.1812
2024.0082136	2024-01-04T12:00:00.000	219.84969256	−60.83174989	219.85019224	−60.82950444	8.1310	6.1903
2024.0109514	2024-01-05T12:00:00.000	219.84968989	−60.83175221	219.85019041	−60.82950632	8.1328	6.1994

Note. The coordinates are apparent coordinates from the location of JWST. The astrometry is available at doi: 10.5281/zenodo.16280658.

ORCID iDs

Charles Beichman https://orcid.org/0000-0002-5627-5471
Aniket Sanghi https://orcid.org/0000-0002-1838-4757
Dimitri Mawet https://orcid.org/0000-0002-8895-4735
Pierre Kervella https://orcid.org/0000-0003-0626-1749
Kevin Wagner https://orcid.org/0000-0002-4309-6343
Billy Quarles https://orcid.org/0000-0002-9644-8330
Jack J. Lissauer https://orcid.org/0000-0001-6513-1659
Max Sommer https://orcid.org/0000-0003-4761-5785
Mark Wyatt https://orcid.org/0000-0001-9064-5598
Nicolas Godoy https://orcid.org/0000-0003-0958-2150
William O. Balmer https://orcid.org/0000-0001-6396-8439
Laurent Pueyo https://orcid.org/0000-0003-3818-408X
Jorge Llop-Sayson https://orcid.org/0000-0002-3414-784X
Jonathan Aguilar https://orcid.org/0000-0003-3184-0873
Rachel Akeson https://orcid.org/0000-0001-9674-1564
Ruslan Belikov https://orcid.org/0000-0002-4951-8025
Anthony Boccaletti https://orcid.org/0000-0001-9353-2724
Elodie Choquet https://orcid.org/0000-0002-9173-0740
Edward Fomalont https://orcid.org/0000-0002-9036-2747
Thomas Henning https://orcid.org/0000-0002-1493-300X
Dean Hines https://orcid.org/0000-0003-4653-6161
Renyu Hu https://orcid.org/0000-0003-2215-8485
Jarron Leisenring https://orcid.org/0000-0002-0834-6140
James Mang https://orcid.org/0000-0001-5864-9599
Michael Ressler https://orcid.org/0000-0001-5644-8830
Eugene Serabyn https://orcid.org/0009-0009-2491-0694
Pascal Tremblin https://orcid.org/0000-0001-6172-3403
Marie Ygouf https://orcid.org/0000-0001-7591-2731
Mantas Zilinskas https://orcid.org/0000-0002-8749-823X

References

Akeson, R., Beichman, C., Kervella, P., et al. 2021, AJ, 162, 14
Astropy Collaboration, Price-Whelan, A. M., Lim, P. L., et al. 2022, ApJ, 935, 167
Batalha, N. E., Marley, M. S., Lewis, N. K., & Fortney, J. J. 2019, ApJ, 878, 170
Bayo, A., Rodrigo, C., Barrado, Y., Navascués, D., et al. 2008, A&A, 492, 277
Beichman, C., Ygouf, M., Llop Sayson, J., et al. 2020, PASP, 132, 015002
Beichman, C. A., Bryden, G., Rieke, G. H., et al. 2005, ApJ, 622, 21160
Bendek, E. A., Belikov, R., Sirbu, D., et al. 2021, Proc. SPIE, 11823, 1182311
Birkby, J., & Parker, L. 2024, in EAS2024, European Astronomical Society Annual Meeting, 2555
Blunt, S., Nielsen, E. L., De Rosa, R. J., et al. 2017, AJ, 153, 229
Blunt, S., Wang, J. J., Angelo, I., et al. 2020, AJ, 159, 89
Boccaletti, A., Cossou, C., Baudoz, P., et al. 2022, A&A, 667, A165
Boccaletti, A., Lagage, P.-O., Baudoz, P., et al. 2015, PASP, 127, 633
Brooke, T. Y. 2003, Main Belt Asteroids in Spitzer Observations, v3.0, https://irsa.ipac.caltech.edu/data/SPITZER/docs/files/spitzer/asteroid_memo.pdf
Buser, R., & Kurucz, R. L. 1992, A&A, 264, 557
Bushouse, H., Eisenhamer, J., Dencheva, N., et al. 2022, JWST Calibration Pipeline, v1.7.0, Zenodo, doi: 10.5281/zenodo.7038885
Brandt, T. D. 2024, PASP, 136, 045004
Butler, R. P., Bedding, T. R., Kjeldsen, H., et al. 2004, ApJL, 600, L75
Carter, A., Kammerer, J., Leisenring, J., et al., 2025 spaceKLIP: JWST Coronagraphy data Data Reduction and Analysis Pipeline, Astrophysics Source Code Library, ascl:2502.014
Carter, A. L., Hinkley, S., Kammerer, J., et al. 2023, ApJL, 951, L20
Castelli, F., & Kurucz, R. L. 2003, in IAU Symp. 210, Modelling of Stellar Atmospheres, 210 ed. N. Piskunov, W. W. Weiss, & D. F. Gray (San Francisco, CA: ASP), A20
Chauvin, G., Videla, M., Beust, H., et al. 2023, A&A, 675, A114
Christiansen, J. L., McElroy, D. L., Harbut, M., et al. 2025, arXiv:2506.03299
Cuello, N., & Sucerquia, M. 2024, Univ, 10, 64
Crotts, K. A., Carter, A. L., Lawson, K., et al. 2025, ApJ, 987, 41
Dohnanyi, J. S. 1969, JGR, 74, 2531
Ducati, J. R. 2002, yCat, 2237, 0
Dupuy, T. J., Kraus, A. L., Kratter, K. M., et al. 2022, MNRAS, 512, 648
Engels, D., Sherwood, W. A., Wamsteker, W., et al. 1981, A&AS, 45, 5
Ertel, S., Defrère, D., Hinz, P., et al. 2018, AJ, 155, 194
Ertel, S., Defrère, D., Hinz, P., et al. 2020, AJ, 159, 177
Farihi, J., Su, K. Y. L., Melis, C., et al. 2025, ApJL, 981, L5
Feroz, F., Hobson, M. P., & Bridges, M. 2009, MNRAS, 398, 1601
Foreman-Mackey, D., Hogg, D. W., Lang, D., et al. 2013, PASP, 125, 306
Gaia Collaboration, Prusti, T., de Bruijne, J. H. J., et al. 2016, A&A, 595, A1
Harris, C. R., Millman, K. J., van der Walt, S. J., et al. 2020, Natur, 585, 357
Huang, X., & Ji, J. 2022, AJ, 164, 177

Hunter, J. D. 2007, CSE, 9, 90
Ito, T., & Ohtsuka, K. 2020, in 14th Europlanet Science Congress 2020, EPSC2020–269
Johnson, R. G., & McClure, B. T. 1976, QuRes, 6, 325
Kammerer, J., Girard, J., Carter, A. L., et al. 2022, Proc. SPIE, 12180, 121803N
Kelsall, T., Weiland, J. L., Franz, B. A., et al. 1998, ApJ, 508, 44
Kennedy, G. M., Matrà, L., Marmier, M., et al. 2015, MNRAS, 449, 3121
Kennedy, G. M., Wyatt, M. C., Su, K. Y. L., et al. 2011, MNRAS, 417, 2281
Kervella, P., Bigot, L., Gallenne, A., et al. 2017, A&A, 597, A137
Kervella, P., Mignard, F., Mérand, A., & Thévenin, F. 2016, A&A, 594, A107
Kozai, Y. 1962, AJ, 67, 591
Kraus, A. L., Ireland, M. J., Huber, D., Mann, A. W., & Dupuy, T. J. 2016, AJ, 152, 8
Kuchner, M., 2012 ZODIPIC: Zodiacal Cloud Image Synthesis, Astrophysics Source Code Library, ascl:1202.002
Lacy, B., & Burrows, A. 2023, ApJ, 950, 8
Lajoie, C.-P., Lallo, M., Meléndez, M., et al. 2023, Technical Report, JWST-STScI-008497
Leggett, S. K., & Tremblin, P. 2023, ApJ, 959, 86
Leggett, S. K., & Tremblin, P. 2024, RNAAS, 8, 13
Leggett, S. K., Tremblin, P., Phillips, M. W., et al. 2021, ApJ, 918, 11
Lester, K. V., Dupuy, T. J., Kraus, A. L., et al. 2023, AJ, 166, 166
Li, L., Jiang, X., & West, R. A. 2018, NatCo, 9, 3709
Lidov, M. L. 1962, P&SS, 9, 719
Lissauer, J. J., Marcy, G. W., Bryson, S. T., et al. 2014, ApJ, 784, 44
Luhman, K. L., Tremblin, P., Alves de Oliveira, C., et al. 2024, AJ, 167, 5
Marley, M. S., Saumon, D., Visscher, C., et al. 2021, ApJ, 920, 85
Mawet, D., Milli, J., Wahhaj, Z., et al. 2014, ApJ, 792, 97
Meisner, A. M., Leggett, S. K., Logsdon, S. E., et al. 2023, AJ, 166, 57
Moe, M., & Kratter, K. M. 2021, MNRAS, 507, 3593
Morley, C. V., Marley, M. S., Fortney, J. J., et al. 2014, ApJ, 787, 78
Mukherjee, S., Batalha, N. E., Fortney, J. J., & Marley, M. S. 2023, ApJ, 942, 71
Mukherjee, S., Fortney, J. J., Morley, C. V., et al. 2024, ApJ, 963, 73
Müller, S., Baron, J., Helled, R., et al. 2024, A&A, 686, A296
Murakami, H., Baba, H., Barthel, P., et al. 2007, PASJ, 59, S369
Naoz, S. 2016, ARA&A, 54, 441
Olnon, F. M., Raimond, E., Neugebauer, G., et al. 1986, A&A, 65, 607
Peale, S. J., & Cassen, P. 1978, Icar, 36, 245
Perrin, M. D., Pueyo, L., Van Gorkom, K., et al. 2018, Proc. SPIE, 9143, 1069809
Perrin, M. D., Sivaramakrishnan, A., Lajoie, C.-P., et al. 2014, Proc. SPIE, 9143, 91433X
Phillips, M. W., Tremblin, P., Baraffe, I., et al. 2020, A&A, 637, A38
Planck Collaboration, Ade, P. A. R., Aghanim, N., et al. 2016, A&A, 586, A132
Polletta, M., Tajer, M., Maraschi, L., et al. 2007, ApJ, 663, 81
Quarles, B., & Lissauer, J. J. 2016, AJ, 151, 111
Quarles, B., & Lissauer, J. J. 2018, AJ, 155, 130
Quarles, B., Lissauer, J. J., & Kaib, N. 2018, AJ, 155, 64
Quirrenbach, A. 2022, RNAAS, 6, 56
Rieke, G., & Gautier, N. 2004, Spitzer Proposal, 52
Rigby, J., Perrin, M., McElwain, M., et al. 2023, PASP, 135, 048001
Rein, H., & Liu, S.-F. 2012, A&A, 537, A128
Rein, H., Tamayo, D., & Brown, G. 2019, MNRAS, 489, 4632
Rieke, G. H., Ressler, M. E., Morrison, J. E., et al. 2015, PASP, 127, 665
Sanghi, A., Beichman, C., Mawet, D., et al. 2025a, RNAAS, 9, 119
Sanghi, A., Beichman, C., Mawet, D., et al. 2025b, ApJL, 989, L23
Soummer, R., Pueyo, L., & Larkin, J. 2012, ApJL, 755, L28
STScI Development Team, 2013 pysynphot: Synthetic Photometry Software Package, Astrophysics Source Code Library, ascl:1303.023
Rigley, J. K., & Wyatt, M. C. 2020, MNRAS, 497, 1143
Sommer, M., Wyatt, M., & Han, Y. 2025, MNRAS, 539, 439
Stone, M. A., Alberts, S., Rieke, G. H., et al. 2024, ApJ, 972, 62
Sullivan, K., Kraus, A. L., Berger, T. A., et al. 2024, AJ, 168, 129
Tabur, V., Bedding, T. R., Kiss, L. L., et al. 2009, MNRAS, 400, 1945
Thebault, P., Kral, Q., & Olofsson, J. 2021, A&A, 646, A173
Trilling, D. E., Stansberry, J. A., Stapelfeldt, K. R., et al. 2007, ApJ, 658, 1289
Tuthill, P., Bendek, E., Guyon, O., et al. 2018, Proc. SPIE, 10701, 107011J
Valenti, J. A., & Fischer, D. A. 2005, ApJS, 159, 141
Virtanen, P., Gommers, R., Oliphant, T. E., et al. 2020, NatMe, 17, 261
von Zeipel, H. 1910, AN, 183, 345
Wiegert, J., Liseau, R., Thébault, P., et al. 2014, A&A, 563, A102
Wagner, K., Boehle, A., Pathak, P., et al. 2021, NatCo, 12, 922
Wogan, N. F., Mang, J., Batalha, N. E., et al. 2025, RNAAS, 9, 108
Wittenmyer, R. A., Butler, R. P., Tinney, C. G., et al. 2016, ApJ, 819, 28
Wright, G. S., Wright, D., Goodson, G. B., et al. 2015, PASP, 127, 595
Wyatt, M. C. 2005, A&A, 433, 1007
Wyatt, M. C., Clarke, C. J., Booth, M., et al. 2011, CeMDA, 111, 1
Xuan, J. W., & Wyatt, M. C. 2020, MNRAS, 497, 2096
Yelverton, B., Kennedy, G. M., Su, K. Y. L., & Wyatt, M. C. 2019, MNRAS, 488, 3588
Zhang, M., & Kainulainen, J. 2022, MNRAS, 517, 5180
Zhao, L., Fischer, D. A., Brewer, J., et al. 2018, AJ, 155, 24